

# ON THE CLUSTER PHYSICS OF SUNYAEV-ZEL'DOVICH AND X-RAY SURVEYS IV: CHARACTERIZING DENSITY AND PRESSURE CLUMPING DUE TO INFALLING SUBSTRUCTURES

N. BATTAGLIA<sup>1</sup>, J. R. BOND<sup>2</sup>, C. PFROMMER<sup>3</sup>, J. L. SIEVERS<sup>4,5</sup>

<sup>1</sup> McWilliams Center for Cosmology, Carnegie Mellon University, Department of Physics, 5000 Forbes Ave., Pittsburgh PA, USA, 15213; nbattaglia@cmu.edu

<sup>2</sup> Canadian Institute for Theoretical Astrophysics, 60 St George, Toronto ON, Canada, M5S 3H8

<sup>3</sup> Heidelberg Institute for Theoretical Studies, Schloss-Wolfsbrunnenweg 35, D-69118 Heidelberg, Germany; christoph.pfrommer@h-its.org

<sup>4</sup> Joseph Henry Laboratories of Physics, Jadwin Hall, Princeton University, Princeton NJ, USA, 08544

<sup>5</sup> Department of Chemistry and Physics, University of Kwa-Zulu Natal, University Road, Westville, KZN, South Africa

Submitted to *ApJ*

## ABSTRACT

Understanding the outskirts of galaxy clusters at the virial radius ( $R_{200}$ ) and beyond is critical for an accurate determination of cluster masses, structure growth, and to ensure unbiased cosmological parameter estimates from cluster surveys. This problem has drawn renewed interest due to recent determinations of gas mass fractions beyond  $R_{200}$ , which appear to be considerably larger than the cosmic mean, and because the clusters' total Sunyaev-Zel'dovich flux receives a significant contribution from these regions. Here, we use a large suite of cosmological hydrodynamical simulations to study the clumpiness of density and pressure and employ different variants of simulated physics, including radiative gas physics and thermal feedback by active galactic nuclei. We find that density and pressure clumping closely trace each other as a function of radius, but the bias on density remains on average  $< 20\%$  within the virial radius  $R_{200}$  (if we only account for the X-ray emitting gas with  $T \gtrsim 10^6$  K). At larger radius, clumping increases steeply due to the continuous infall of coherent structures that have not yet passed the accretion shock. Density and pressure clumping increase with cluster mass and redshift, which probes on average dynamically younger objects that are still in the process of assembling. The angular power spectra of gas density and pressure show that the clumping signal is dominated by comparably large substructures with scales  $\gtrsim R_{200}/5$ , signaling the presence of gravitationally-driven "super-clumping". In contrast, the angular power spectrum of the dark matter (DM) shows an almost uniform size distribution due to unimpeded subhalos. The quadrupolar anisotropy dominates the signal and correlates well across different radii as a result of the prolateness of the DM potential. At smaller angular scales, gas density and pressure at different radii lose coherence due to dissipative gas physics. We provide a synopsis of the radial dependence of the clusters' non-equilibrium measures (kinetic pressure support, ellipticity, and clumping) that all increase sharply beyond  $R_{200}$ .

*Subject headings:* Galaxies: Clusters: General — Large-Scale Structure of Universe — Methods: Numerical — Cosmic Microwave Background — Cosmology: Theory

## 1. INTRODUCTION

Clusters are the largest and latest objects in the universe that had time to collapse under the influence of their gravity, sitting atop the mass hierarchy. They form at sites of constructive interference of long waves in the primordial density fluctuations, the coherent peak-patches (Bardeen et al. 1986; Bond & Myers 1996). Since the probability of such events is exponentially suppressed for larger objects and redshifts, clusters are rare events. Hence, they are very sensitive tracers of the growth of structure in the universe and the cosmological parameters governing it (as demonstrated by recent measurements, e.g., by Allen et al. 2008; Vikhlinin et al. 2009; Mantz et al. 2010; Hajian et al. 2013; Mantz et al. 2014). Most of the cluster mass is in form of dark matter (DM) while the dominating fraction of cluster baryons is in the form of a hot ( $kT \sim (1-10)$  keV) diffuse plasma, the intra-cluster medium (ICM), with the remaining baryons residing in the clusters' numerous stars and galaxies.

Recent X-ray observations from *Chandra* and *XMM-Newton* have witnessed a rich and complicated picture of the ICM in the interiors of clusters—many ostensibly "relaxed" clusters show substantial small-scale variation in temperature, metallicity, and surface brightness (e.g., Fabian et al. 2011; Churazov et al. 2012). These effects seem to be driven by non-gravitational feedback processes in the cluster centers

(McNamara & Nulsen 2007) or are remnant features of cluster mergers that are either caught in the process of dissipating the gravitational binding energy or at a later relaxation stage that is characterized by sloshing motions. On increasingly larger scales, the mostly dark-matter (DM) dominated gravity of the overall cluster potential starts to dominate the dynamics of the hot baryons; so the hope is that on large enough scales the influence of those non-gravitational (gastrophysical) effects is minimized. However, when approaching the cluster outskirts, we encounter other complications that are predicated upon the mass assembling history of clusters, with an increasing level of kinetic pressure support (e.g., Evrard 1990; Rasia et al. 2004; Lau et al. 2009; Vazza et al. 2009; Battaglia et al. 2010; Nelson et al. 2012; Battaglia et al. 2012a), ellipticity (e.g., Kasun & Evrard 2005; Macciò et al. 2008; Lau et al. 2011; Battaglia et al. 2012a), and density clumping (e.g., Nagai & Lau 2011; Zhuravleva et al. 2013; Khedekar et al. 2013; Roncarelli et al. 2013; Vazza et al. 2013; Avestruz et al. 2014).

Until recently, we did not have the possibility of directly observing the ICM outskirts because of their low densities that escaped detections by means of thermal X-ray bremsstrahlung emission which scales with the square of the gas density. The high and temporarily variable particle background of *Chandra* and *XMM-Newton* also provided a fundamental limit to the sensitivity of X-ray emission in the ICM outskirts. A complemen-

tary probe of the ICM is the thermal Sunyaev-Zel'dovich (SZ) effect, the Compton up-scattering of cosmic microwave background (CMB) photons by hot electrons with its unique signature of a spatially-varying distortion of the CMB spectrum, a decrement in thermodynamic temperature at frequencies below  $\sim 220$  GHz, and an excess above (Sunyaev & Zeldovich 1970). But similarly to X-ray observations, detecting ICM in cluster outskirts also remained a challenge to SZ experiments despite their intrinsic advantage to characterize those regions because the signal scales with the line-of-sight integral of the free electron pressure. However, SZ observations of low surface brightness outskirts are predicated upon the ability to separate the SZ signal from the primary anisotropies of the CMB (as well as the contribution due to radio and dusty galaxies) and requires comparably sensitive multi-frequency observations that allow to cleanly separate the SZ signal owing to its unique spectra signature.

Those outskirts are of particular importance since they connect the cluster interior to the filamentary cosmic web with its warm-hot intergalactic medium that is expected to host half of today's baryon budget. Hence, improving our understanding of the dynamical state of the ICM in cluster outskirts helps unraveling cluster masses and cosmological structure formation. Precise characterization of the clumpiness of the ICM density and pressure will be of crucial importance for current and next generation surveys in the X-rays (*eROSITA*) and those employing the SZ effect (*Atacama Cosmology Telescope* (ACT, Fowler et al. 2007), *South Pole Telescope* (SPT, Carlstrom et al. 2011), and *Planck* as will be separably laid out in the following.

### 1.1. Density clumping and X-ray inferred gas mass fractions

The launch of the *Suzaku* X-ray observatory opened the window for studies of cluster outskirts due to its low-Earth orbit that ensures a low and stable particle background. Recent *Suzaku* observations detected cluster X-ray emission up to and even beyond  $R_{200}$  and consistently find decreasing temperature profiles towards larger radii, in accordance with theoretical expectations. However, the majority of them observes an excess X-ray emission for radii  $\gtrsim R_{500}$  over what is expected from cosmological hydrodynamical simulations at different levels of significance (e.g., George et al. 2009; Bautz et al. 2009; Reiprich et al. 2009; Hoshino et al. 2010; Kawaharada et al. 2010; Akamatsu et al. 2011; Simionescu et al. 2011; Walker et al. 2012; Sato et al. 2012; Urban et al. 2014).

This has been interpreted as entropy profiles which rise in the outskirts less steeply than the predictions of hydrodynamical simulations (almost independent of the adopted physics) or an increasing profile of the enclosed gas mass fraction,  $f_{\text{gas}} = M_{\text{gas}}/M_{\text{tot}}$ , to values above the universal Hubble-volume-smoothed proportion. While some of that excess can be attributed to the anisotropic nature of the cosmic web that connects to the outer cluster parts (Battaglia et al. 2013), there remain other possible explanations. Those include an increasing kinetic pressure contribution in the outskirts, which biases hydrostatic mass estimates of clusters low and gas mass fractions high. Similarly, it was argued that the presence of substantial density clumping (e.g., Eckert et al. 2013; Morandi & Cui 2014) can bias X-ray inferred densities and, hence, gas mass fractions high (e.g., Nagai & Lau 2011; Khedekar et al. 2013; Roncarelli et al. 2013; Battaglia et al. 2013) as well as entropy

values low.<sup>1</sup>

### 1.2. Pressure clumping and Sunyaev-Zel'dovich observations

Pressure clumping could have important influences on determinations of SZ scaling relations and the SZ power spectrum (or its interpretation in terms of cosmology). There is currently great interest in measuring the SZ power spectrum, which is an integral of the cluster mass function times the square of the Fourier transform of the average pressure profile of clusters/groups. Since radiative physics in combination with non-gravitational energy injection strongly modifies the pressure profile and since the SZ power spectrum depends sensitively on the *rms* amplitude of the (linear) density power spectrum on cluster-mass scales,  $\sigma_8$ , this is potentially a great tool to simultaneously constrain cluster physics and cosmology. Thus far, *ACT* and *SPT* have detected the SZ effect in the CMB power spectrum (e.g., Reichardt et al. 2012; Sievers et al. 2013) and used SZ detected clusters to constraints cosmological parameters (e.g., Reichardt et al. 2013; Hasselfield et al. 2013). Additionally, the *Planck Collaboration* has released several papers on SZ science, including scaling relations (e.g., Planck Collaboration et al. 2011c,a,d,b), pressure profiles (Planck Collaboration et al. 2013c), cosmological constraints from SZ clusters (Planck Collaboration et al. 2013a) and SZ power spectrum measurements at small multipoles (Planck Collaboration et al. 2013b).

Significant pressure clumping would impact the SZ power spectrum on different angular scales depending on the physical scale of clumping and its strength as well as the cluster redshift. Pressure clumping at radii  $> R_{500}$  manifests itself on angular multipoles  $\ell \lesssim 4000$ , which corresponds to angular scales  $\gtrsim 2.5$  arcmin (Battaglia et al. 2012b). For example, at  $\ell \simeq 1000$  more than 40% of the power is contributed from radii  $> R_{500}$ . However, the largest impact on the SZ power spectrum originates from clumps within  $R_{500}$  that carry a larger SZ signal than their analogues at larger radii due to a combination of ram-pressure and adiabatic compression of infalling substructures and an increasing pressure toward the cluster center that amplifies any deviations from spherical symmetry. This can be indirectly inferred from the differences between the simulated SZ power spectrum and the model that pastes a smoothed fit to the sphericalized pressure profile in the simulations; see Figures 7 and 8 of Battaglia et al. (2012b). If semi-analytical SZ power spectrum templates neglect this contribution from clumping, the resulting cosmological parameters would be biased, or, if sufficient freedom was left to address these uncertainties in the cluster physics, this would limit the accuracy of the cosmological parameter estimation.

More than half of the total SZ flux accumulates from radii  $> R_{500}$  (Battaglia et al. 2010). If there are significant pressure fluctuations present on these scales, this could change the interpretation of detected signal strength in the presence of a noisy background, in particular when extrapolating pseudo-pressure profiles that are informed by X-ray observations of the more homogeneous inner regions (e.g., Arnaud et al. 2010). This could potentially bias inferred SZ fluxes and resulting scaling relations, especially in lower angular resolution surveys such as *Planck* that rely on accurate templates for signal detection.

<sup>1</sup> Observational or instrumental systematics for the observed excess emission (which is typically a factor of 3-5 below the soft extragalactic X-ray background) include fluctuations of unresolved point sources, point-spread function leakage from masked point sources, or stray light from the bright inner cluster core. This was argued not to be responsible for the excess emission (e.g., Simionescu et al. 2011).

### 1.3. Overview

Those points provide ample motivation for characterizing density and pressure clumping as a function of cluster mass, radius, and physics as well as understanding its origin. It seems to be crucial to accurately model its contribution to get unbiased cosmological constraints in future X-ray and SZ surveys. To this end it is not sufficient to look at a small sample of simulated clusters, but rather to use a large statistical sample drawn from comparably large cosmological volumes to accurately address the cluster-to-cluster scatter. However, such an undertaking dictates the limiting resolution (for a given volume and particle number) that is far larger than the desired resolution needed to follow all the possibly necessary physics. We hence concentrate on modeling the most important physical agents with physically motivated subgrid models and carefully check numerical convergence and whether we obtain agreement with observed integrated quantities such as gas and stellar masses, SZ scaling relations and SZ power spectra to gain confidence to our effective model. Due to uncertainties of the subgrid modeling of cluster physics, it appears also critical to complement such an approach with different model variants that enable to develop an intuition about the effect of differently modeled physics on various observables.

This is the forth paper of a series of papers addressing the cluster physics of SZ and X-ray surveys. In the first two companion papers, we thoroughly scrutinized the influence of feedback, non-thermal pressure and cluster shapes on  $Y-M$  scaling relations (Battaglia et al. 2012a, hereafter BBPS1) and the thermal SZ power spectrum (Battaglia et al. 2012b, hereafter BBPS2). The third paper details the measurement biases and cosmological evolution of gas and stellar mass fractions (Battaglia et al. 2013, hereafter BBPS3), and the fifth provides an information theoretic view of clusters and their non-equilibrium entropies (Battaglia et al. 2014, hereafter BBPS5).

The outline of this paper is as follows. In Section 2, we introduce our simulations and the subgrid physics models. In Section 3, we study how density and pressure clumping varies with radius, cluster mass, redshift, and simulated physics. In Section 4, we study the origin of clumping by computing dark matter and gas mass as well as thermal energy distributions in angular cones and by cross-correlating their distributions. In Section 5, we provide a synthesis of the different non-equilibrium measures in cluster outskirts, such as kinetic pressure contribution, ellipticity, and clumping, that all are predicated upon the mass assembling history of clusters. We conclude in Section 6.

## 2. COSMOLOGICAL SIMULATIONS AND CLUSTER SAMPLE

We use smoothed particle hydrodynamic (SPH) simulations of large-scale periodic boxes of cosmological volume, which provide us with large cluster samples to accurately characterize ICM properties over large ranges of cluster masses and redshifts. We use a modified version of the GADGET-2 (Springel 2005) code. Our sequence of periodic boxes have lengths of 165 and 330  $h^{-1}$  Mpc, which are filled with  $N_{\text{DM}} = N_{\text{gas}} = 256^3$  and  $512^3$  dark matter (DM) and gas particles, respectively. This choice maintains the same gas particle mass  $m_{\text{gas}} = 3.2 \times 10^9 h^{-1} M_{\odot}$ , DM particle mass  $m_{\text{DM}} = 1.54 \times 10^{10} h^{-1} M_{\odot}$  and a minimum gravitational smoothing length  $\varepsilon_s = 20 h^{-1}$  kpc for different computational volumes. We compute SPH densities with 32 neighbour particles. For our standard calculations, we adopt a tilted  $\Lambda$ CDM cosmology, with total matter density (in units of the critical)  $\Omega_m = \Omega_{\text{DM}} + \Omega_b = 0.25$ , baryon density

$\Omega_b = 0.043$ , cosmological constant  $\Omega_{\Lambda} = 0.75$ , Hubble parameter  $h = 0.72$  in units of 100 km  $s^{-1}$  Mpc $^{-1}$ , spectral index of the primordial power-spectrum  $n_s = 0.96$  and  $\sigma_8 = 0.8$ .

We show results from simulations employing three different variants of simulated physics: the first only accounts for gravitational physics such that the gas entropy can only increase through *shock heating*; the second model additionally accounts for *radiative cooling*, star formation, thermal energy feedback by supernovae, galactic winds, and cosmic-ray physics; and the last model additionally accounts for thermal *feedback by active galactic nuclei (AGNs)*. Radiative cooling and heating were computed assuming an optically thin gas of primordial hydrogen and helium composition in a time-dependent, spatially uniform ultraviolet background. Star formation and thermal feedback by supernovae were modelled using the hybrid multiphase model for the interstellar medium of Springel & Hernquist (2003). The CR population is modelled as a relativistic proton population, which has an isotropic power-law distribution function in momentum space with a spectral index of  $\alpha = 2.3$  and only accounts for CR acceleration at cosmological structure formation shocks, following Pfrommer et al. (2006); Enßlin et al. (2007); Jubelgas et al. (2008). With those parameters, the CR pressure modifies the SZ effect at most at the percent level, which is just consistent with the latest cluster gamma-ray limits (Ackermann et al. 2013; Arlen et al. 2012; Aleksić et al. 2012) and causes a similarly small reduction of the resulting integrated Compton- $y$  parameter (Pfrommer et al. 2007). The AGN feedback prescription included in the simulations (for more details see Battaglia et al. 2010) enables lower computational resolution and hence can be applied to large-scale structure simulations. It couples the black hole accretion rate to the global star formation rate (SFR) of the central region of the cluster, as inspired by a model of Thompson et al. (2005). The thermal energy is injected into the ICM such that it is proportional to the stellar mass formed within a given central spherical region.

We use a two-step algorithm to compute the virial mass of a cluster. First, we find all clusters in a given snapshot using a friends-of-friends (FOF) algorithm. Second, using a spherical overdensity method with the FOF values as starting estimates, we recursively calculate the center of mass, the virial radius,  $R_{\Delta}$ , and mass,  $M_{\Delta}$ , contained within  $R_{\Delta}$ . The radially averaged profiles of a given quantity are computed as a function of cluster-centric radii, which are scaled by  $R_{\Delta}$ . We define  $R_{\Delta}$  as the radius at which the mean interior density equals  $\Delta$  times the *critical density* of the universe, e.g., for  $\Delta = 200$  or 500. Our cluster sample (for each simulation type) has  $\simeq 1300$  clusters with  $M_{200} > 7 \times 10^{13} M_{\odot}$  and  $\simeq 800$  clusters with  $M_{200} > 1 \times 10^{14} M_{\odot}$  at  $z = 0$ .

## 3. CLUMPING FACTORS

### 3.1. Definitions and SPH volume bias

We define the dimensionless  $n$ -th order moments of mass density ( $\rho$ ) and thermal pressure ( $P_{\text{th}}$ ) by

$$\tilde{C}_{n,\rho} = \frac{\langle \rho^n \rangle}{\langle \rho \rangle^n} \quad \text{and} \quad \tilde{C}_{n,P} = \frac{\langle P_{\text{th}}^n \rangle}{\langle P_{\text{th}} \rangle^n}, \quad (1)$$

where  $n \in \mathbb{Z}$ . Since mass density and thermal pressure are both intensive thermodynamic quantities, averages are always volume averages, i.e., the  $n$ -th order moments of mass density and

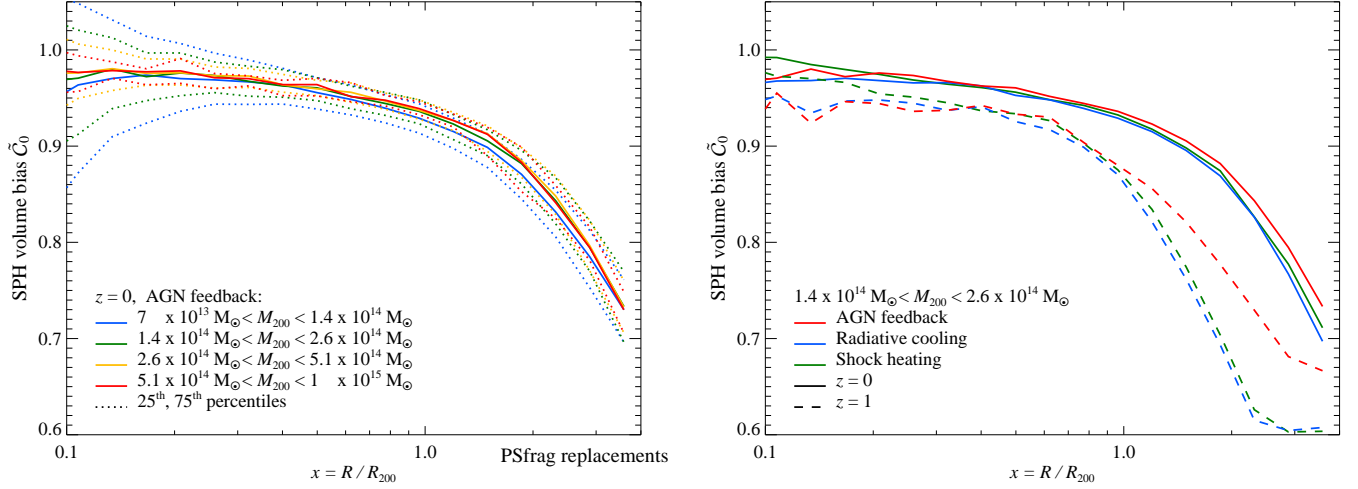


**Figure 1.** Radial dependence of the SPH volume bias,  $\tilde{C}_0 = \sum_i V_i/V$ , which is given by the ratio of the sum of volume elements occupied by SPH particles ( $V_i$ ) and the true volume of the concentric shell ( $V$ ). Left: median (solid) and percentile profiles (dotted) of  $\tilde{C}_0$  for different cluster mass ranges in our AGN feedback model at  $z=0$ . Right: median profile of  $\tilde{C}_0$  for different physics models at  $z=0$  and  $z=1$  for cluster masses  $1.4 \times 10^{14} M_\odot < M_{200} < 2.6 \times 10^{14} M_\odot$ . The influence of the SPH volume bias becomes progressively greater for larger radii and is softened in our AGN feedback model for  $R > R_{200}$ , in particular at  $z \gtrsim 1$ .

thermal pressure within a radial shell are defined by

$$\langle \rho^n \rangle = \frac{1}{V} \sum_i \frac{m_{\text{gas},i}}{\rho_i} \rho_i^n = \frac{1}{V} \sum_i m_{\text{gas},i} \rho_i^{n-1}, \quad (2)$$

$$\langle P_{\text{th}}^n \rangle = \frac{1}{V} \sum_i \frac{m_{\text{gas},i}}{\rho_i} P_{\text{th},i}^n = \frac{1}{V} \sum_i m_{\text{gas},i} \rho_i^{n-1} \left( \frac{kT_i}{\mu m_p} \right)^n, \quad (3)$$

where we sum over all SPH particles with mass  $m_{\text{gas},i}$ , mass density  $\rho_i$ , and temperature  $T_i$  that are within a radial shell of volume  $V$ ,  $\mu$  denotes the mean molecular weight, and  $m_p$  is the proton mass. A particular moment is the zeroth order density moment  $\tilde{C}_0$ , which we will call SPH volume bias for reasons that become clear momentarily,

$$\tilde{C}_0 = \langle 1 \rangle = \frac{1}{V} \sum_i \frac{m_{\text{gas},i}}{\rho_i} = \frac{1}{V} \sum_i V_i. \quad (4)$$

Clearly, we expect this to be identical to unity everywhere. Figure 1 shows this SPH volume bias as a function of radius (scaled by  $R_{200}$ ).<sup>2</sup> While the median of the SPH volume bias is close to unity at small radii, it deviates progressively for larger radii, and starts to severely underpredict unity outside  $R_{200}$ . This is because of the inability to accurately percolate space that is characterized by an inhomogeneous density distribution with a Lagrangian spherical density kernel as realized by SPH. The relative deviation of the SPH volume bias from unity almost doubles at  $z=1$  in comparison to  $z=0$  (with the exception of our AGN feedback model which shows a smaller increase towards  $z=1$ ). The reason for this deviation is a progressively larger inhomogeneity of the ICM for larger radii due to increasing large-scale ellipticity (BBPS1) as well as an increased density clumping (Nagai & Lau 2011, see also below). The right-hand side of Figure 1 shows that the SPH volume bias is almost independent of the simulated physics (especially for  $z=0$ ) and hence is not affected by the presence of the cold

interstellar medium (ISM) of galaxies (see also discussion surrounding Figure 3).

As a result of this volume bias, we decided to redefine the dimensionless  $n$ -th order density and thermal pressure moments and to apply a correction for the SPH volume bias:

$$C_{n,\rho} = \tilde{C}_{n,\rho} \tilde{C}_0^{n-1} \quad \text{and} \quad C_{n,p} = \tilde{C}_{n,p} \tilde{C}_0^{n-1} \quad (5)$$

where the  $\tilde{C}_0$  term has been chosen to cancel each power of the SPH volume in the averaging procedure. While this corrects the median of the  $n$ -th order density or pressure moments (which is our main objective in the present work), it does not correct their entire distributions. We show in Appendix A how this correction impacts clumping factors (second order density moment) and the negative order density moments, which are useful for studying underdense regions. In particular for the latter case, the SPH volume bias correction removes unphysical estimates of the negative order density moments that are smaller than unity.

Previous work on clumping using SPH simulations (Roncarelli et al. 2013) did not account for this volume bias. If we neglected our SPH volume-bias correction, our values for  $C_{2,\rho}$  in the *shock heating-only* model, which are not susceptible to a differing implementation of the sub-grid physics models, agree with those of Roncarelli et al. (2013). This can be seen by comparing  $C_{2,\rho}$  for our massive cluster sample with  $M_{200} > 5.1 \times 10^{14} M_\odot$  (red lines in the middle panel of Figure 3) to Figure 4 in Roncarelli et al. (2013).

### 3.2. Density and pressure clumping

After introducing our definitions and formalism, we turn to estimating the clumping factor for density and pressure distribution. In Figure 2, we show the radial profile of the square root of the density clumping factor,  $\sqrt{C_{2,\rho}}$ . The emissivity of thermal bremsstrahlung scales with the square of the gas density. Hence the X-ray-inferred gas density profile is biased high by  $\sqrt{C_{2,\rho}}$  which increases as a function of cluster mass at

<sup>2</sup> To derive the radial profiles, we choose an equidistant spacing in  $\log R$  and ensured that the ratio of particle smoothing lengths to radial extent of the shells is always smaller than unity in our smallest clusters for  $R > 0.5R_{200}$ .

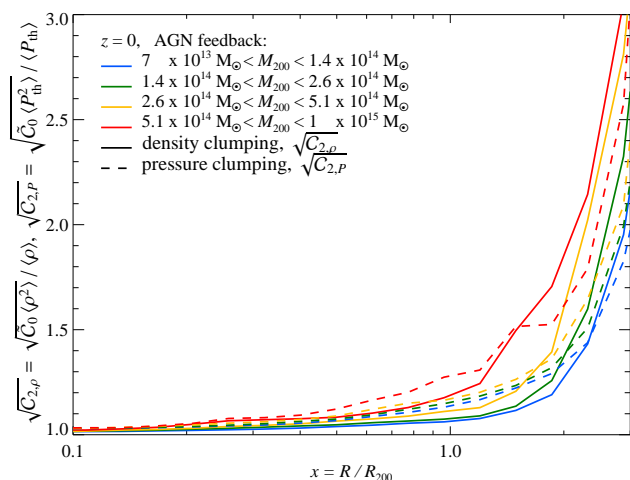


**Figure 2.** Radial profile of the square root of the density clumping factor,  $\sqrt{C_{2,\rho}}$  (solid), and the pressure clumping factor,  $\sqrt{C_{2,p}}$  (dashed), corrected for the SPH volume bias. Shown are the median profiles of the clumping factors for the corresponding cluster mass ranges in our AGN feedback model (indicated by different colors). We impose a temperature cut to the density clumping factor and only consider SPH particles with  $T > 10^6$  K that can be observed by their X-ray emission. The X-ray-inferred gas density profile is biased high by  $\sqrt{C_{2,\rho}}$  which increases as a function of cluster mass at each radius, but remains  $< 1.2$  for  $R < R_{200}$  in all clusters. The pressure clumping dominates over the density clumping inside the virial radius, but increases at a slower rate outside this radius so that the density clumping takes over.

each radius, but remains  $< 1.2$  for  $R < R_{200}$  in all clusters.<sup>3</sup> However,  $\sqrt{C_{2,\rho}}$  increases sharply outside  $R_{200}$ . There is a clear trend of an increasing clumping factor for larger clusters, which have on average higher mass accretion rates, i.e., they are assembling at the current epoch and hence are dynamically younger.

In Figure 2, we additionally show the square root of the pressure clumping factor,  $\sqrt{C_{2,p}}$ . It broadly follows the trend with radius and mass that we observe for density clumping. However, there are small but distinct differences. While pressure clumping dominates over density clumping inside the virial radius, it increases at a slower rate outside this radius and becomes subdominant in comparison to the density clumping. This similar radial behavior argues for a common physical origin and we will come back to this question in Section 4. In contrast to the X-rays, the thermal SZ flux scales with the gas pressure, so the Compton- $\gamma$  maps are not biased by the presence of pressure clumping. There will be a contribution of pressure clumping to the thermal SZ power spectrum, however. The magnitude of this contribution is set by a balance of the overall signal strength (that increases towards the cluster core) and the strength of the clumping signal (that increases for larger radii).

In Figure 2, we applied an observationally motivated temperature cut to the density moments and only considered SPH particles with  $T > 10^6$  K that can be observed by their X-ray emission. We assess the impact of such a temperature cut on density and pressure clumping in Figure 3. Clearly, the density clumping factors are significantly biased high by the presence of the ISM in cluster galaxies as well as cold, dense gas clumps

<sup>3</sup> We note that our clumping statistics only accounts for clumping that we can numerically resolve. In principle, there could be a spectrum of clumps to much smaller masses, but these clumps would have to be non-gravitationally heated to X-ray emitting temperatures. In our simulations, we resolve a  $2 \times 10^{12} M_{\odot}$  object with 100 resolution elements which has the virial temperature  $< 10^6$  K.

that are ram-pressure stripped from galaxies. This bias needs to be accounted for when comparing to X-ray observations by employing, e.g., a temperature cut of  $T > 10^6$  K, which we will adopt for all the density clumping calculations hereafter. We do not include a volume-selection scheme (Roncarelli et al. 2006) in our analysis since the goal of this work is to quantify all ICM inhomogeneities, including large-scale features. This allows us to study the connection to pressure clumping, which is important for improved analyses of SZ data.

Does this temperature floor remove a physically relevant phase of the ICM irrespective of the uncertainty of galaxy formation physics and the associated ISM phase? To answer this, we show the density clumping factors in our simulations with *shock heating-only* in the central panel of Figure 3. We find identical values for  $C_{2,\rho}$  within  $R_{200}$  irrespective of adopting the temperature cut. However, the density clumping factors with a temperature cut are slightly enhanced at large radii  $R \gtrsim 2.5R_{200}$ : the temperature restriction removes gas with the lowest density at any given radius that is neither in self-bound substructures nor has it passed through the final cluster accretion shock. For non-radiative physics, any temperature enhancement is necessarily accompanied by density enhancements by either adiabatic compression or shock heating. Hence removing the temperature and density floor of the warm-hot intergalactic medium leaves the extrema which also slightly increases the resulting density clumping, preferably for low-mass objects. We caution that the inclusion of AGN heating (in addition to radiative cooling and star formation) modifies the pressure and temperature beyond the virial radius and depending on the sign of this change, either enhances or suppresses the differences in the clumping factor (Battaglia et al. 2010).

In contrast to density clumping, pressure clumping in our *AGN feedback* model (right panel, Figure 3) depends very little on any temperature cuts suggesting that these cold gas clumps find themselves in pressure equilibrium with the ambient hot ICM. Qualitatively similar to density clumping in our *shock heating-only* model, we find a slightly larger pressure clumping if we adopt a temperature cut of  $T > 10^6$  K in low-mass systems. This again is due to the colder pre-shock regions of the warm-hot intergalactic medium that realize  $T < 10^6$  K. Hence, in order to compute pressure clumping in the remainder of this work, we do not adopt any temperature cut. This is again observationally motivated as the Compton- $\gamma$  parameter represents the line-of-sight integral over all free electrons.

### 3.3. Impact of simulated physics on clumping

In Figure 4, we show how the radial profiles of density and pressure clumping depend on our different variants of physics. At  $z = 0$ , all different clumping measures are indistinguishable within the cluster-to-cluster scatter. The picture is different at  $z = 1$ , where both clumping measures in our *AGN feedback* model fall short by a factor of two at  $2R_{200}$  in comparison to the clumping factors in the *radiative cooling* and *shock heating-only* simulation. This difference increases for larger radii due to the shallower slope of the clumping factors in the *AGN feedback* models. This is due to the central energy injection in this model that smooths out the central density and pressure values and causes smaller fluctuations with respect to the floor values (Battaglia et al. 2010).

### 3.4. Clumping changes with cluster mass, redshift and dynamical state

In Figures 5 and 6, we show profiles of density and pressure clumping for different cluster masses, redshifts, and dynamical

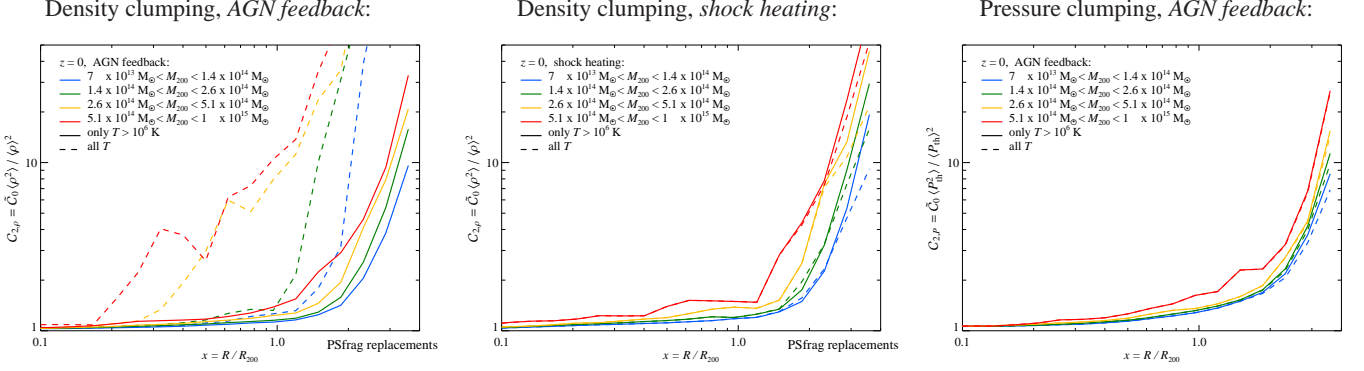


**Figure 3.** Influence of the temperature cut on the density and pressure clumping factors ( $C_{2,\rho}$  and  $C_{2,p}$ ) at  $z=0$ . Left: density clumping factor in our *AGN feedback* model for SPH particles with  $T > 10^6$  K that can be observed by their X-ray emission (solid) and for all particles, i.e., without temperature restrictions (dashed). The cold ISM of cluster galaxies and ram-pressure stripped dense gas clumps from these galaxies bias the density clumping factor high. Center: to address whether the temperature floor removes a physically relevant phase of the ICM, we compare the density clumping factor in our *shock heating-only* model for SPH particles with  $T > 10^6$  K (solid) and for all particles (dashed). Clumping with a temperature cut is only slightly enhanced at large radii  $R \gtrsim 2.5R_{200}$ , implying that our temperature cut does not bias our clumping results at smaller radii with physically relevant substructures. Right: the pressure clumping factor in our *AGN feedback* model for SPH particles with  $T > 10^6$  K (solid) and for all particles (dashed) are similar, suggesting that the dense, cold gas clumps are in pressure equilibrium with the ambient hot ICM.

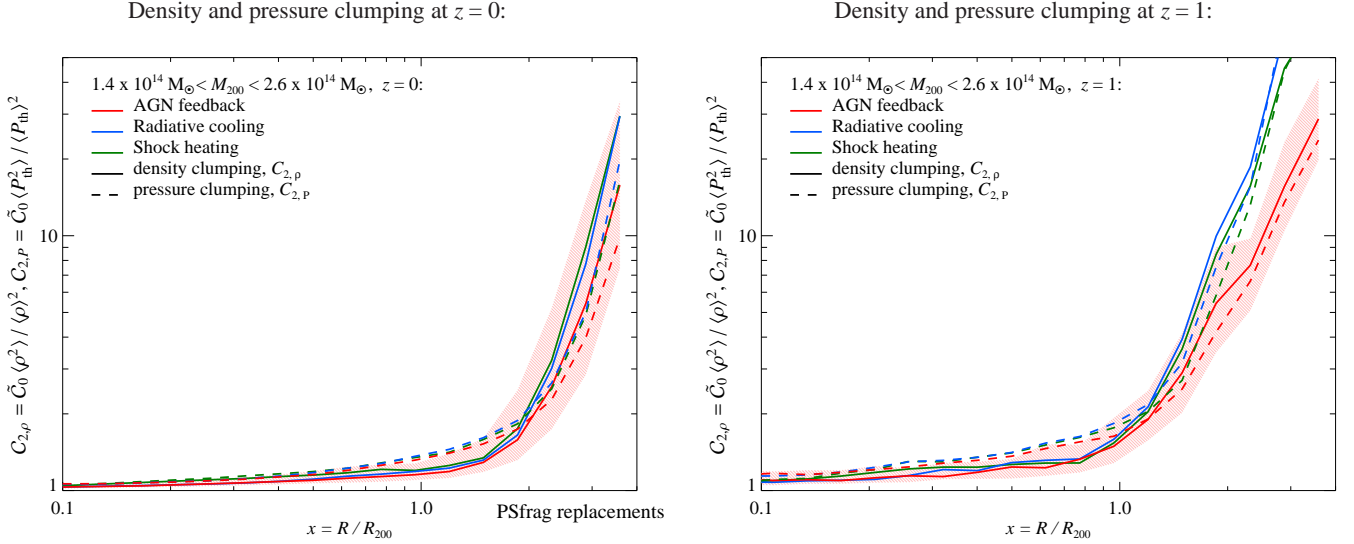


**Figure 4.** Impact of different physics models on the density (solid) and pressure clumping factor (dashed), corrected for the SPH volume bias. We compare the median profiles for our *AGN feedback* model (red with 25<sup>th</sup> and 75<sup>th</sup> percentiles of  $C_{2,\rho}$  shown by the error bands), our simulations with *radiative cooling* and star formation (blue), and with *shock heating-only* (green) at  $z=0$  (left) and  $z=1$  (right). Independent of the simulated physics, the slopes of the radial profiles of  $C_{2,\rho}$  and  $C_{2,p}$  change at  $R \sim 2R_{200}$  ( $z=0$ ) and  $R \sim R_{200}$  ( $z=1$ ). The *AGN feedback* model shows the lowest clumping in density and pressure at each radius.

states. At each radius, density and pressure clumping increases for heavier clusters as well as for larger redshifts (except for the highest cluster mass range of  $5.1 \times 10^{14} M_{\odot} < M_{200} < 1 \times 10^{15} M_{\odot}$  at  $z=1$  where we do not have sufficient statistics). If we identify the clumping with infalling (sub-)structures (see Section 4), then we see that those accreting structures from the cosmic web penetrate to smaller radii in bigger clusters.

The dynamical state of a clusters is determined by the ratio of kinetic-to-thermal energy,  $K/U$ , within  $R_{200}$ . In BBPS3 we show that this tracer correlates with another commonly used tracer known as centroid shift,  $\langle w \rangle$  (Mohr et al. 1993). The internal kinetic energy,  $K$ , and thermal energy,  $U$ , of a cluster are defined as

$$K(< R_{200}) \equiv \sum_i \frac{3m_{\text{gas},i}P_{\text{kin},i}}{2\rho_i}, \quad (6)$$

$$U(< R_{200}) \equiv \sum_i \frac{3m_{\text{gas},i}P_{\text{th},i}}{2\rho_i}, \quad (7)$$

where  $m_{\text{gas}}$  and  $\rho$  are the gas mass and the SPH density, respectively for all particles  $i$  less than  $R_{200}$ ,  $P_{\text{th}} = kT\rho/(\mu m_p)$  denotes the thermal pressure, and the kinetic pressure is defined as

$$P_{\text{kin}} = \rho \delta v^2 / 3, \quad (8)$$

$$\delta \mathbf{v} = a(\mathbf{v} - \bar{\mathbf{v}}) + aH(a)(\mathbf{x} - \bar{\mathbf{x}}). \quad (9)$$

The code uses comoving peculiar velocities, which we convert into the internal cluster velocities relative to the mean cluster velocity in the Hubble flow. Here  $H(a)$  denotes the Hubble function,  $a$  is the scale factor,  $\mathbf{v} (= d\mathbf{x}/dt)$  is the peculiar velocity, and  $\mathbf{x}$  is the comoving position of each particle. The averaged cluster bulk flow for the gas particles is  $\bar{\mathbf{v}}$  and the center of mass is  $\bar{\mathbf{x}}$ , both calculated within  $R_{200}$ .

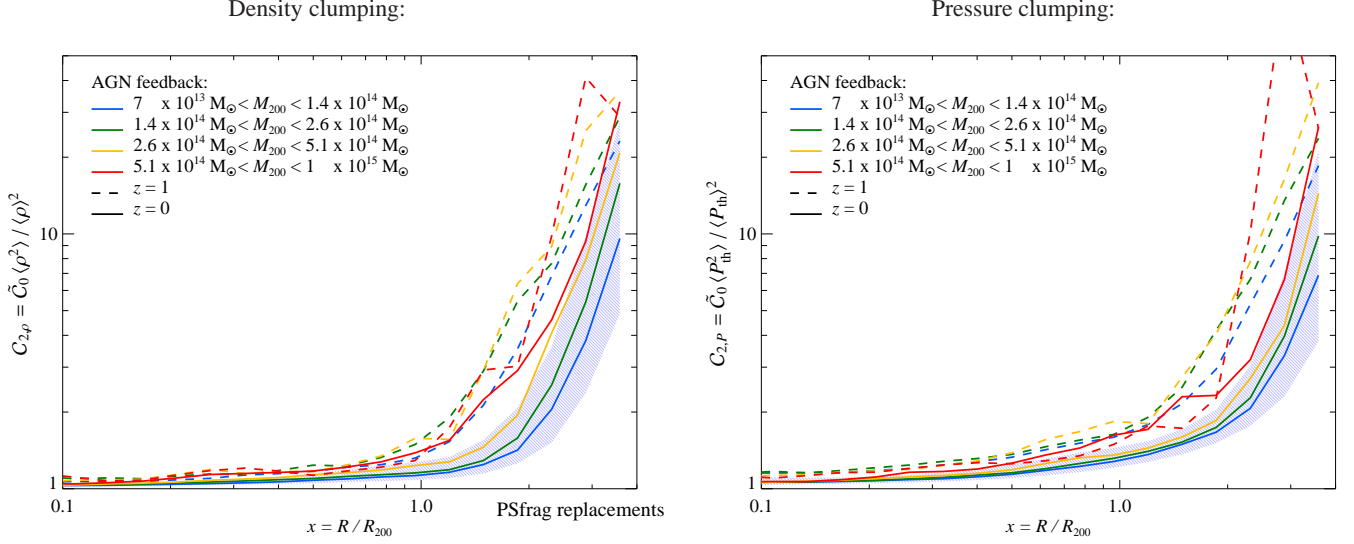


**Figure 5.** Radial profiles of the density (left) and pressure clumping factor (right) for different cluster mass ranges (indicated with different colors). Shown are the median profiles at  $z = 0$  (solid) and  $z = 1$  (dashed) as well as the 25<sup>th</sup> and 75<sup>th</sup> percentiles for the lowest cluster mass range for  $z = 0$  (error bands). At each radius, clumping increases for heavier clusters which assembled on average more recently.

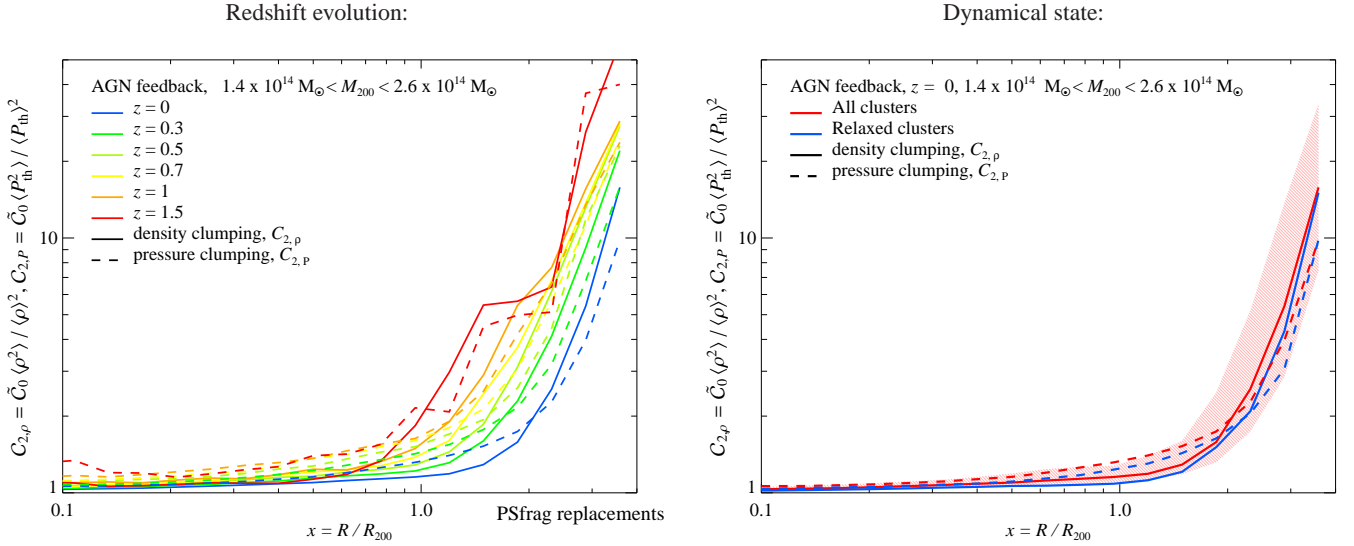


**Figure 6.** Left: redshift evolution of the clumping factor for density (solid) and pressure (dashed). Right: comparison of the density (solid) and pressure (dashed) clumping between a subsample of relaxed clusters (blue, with the lowest ratio of total kinetic-to-thermal energy,  $K/U$ ) and all clusters (red). In both panels, we show the median profiles for our *AGN feedback* model for cluster masses in the range  $1.4 \times 10^{14} M_{\odot} < M_{200} < 2.6 \times 10^{14} M_{\odot}$ . The red band in the right panel represents the range from the 25<sup>th</sup> to 75<sup>th</sup> percentile of the sample that includes all the clusters.

The ratio  $K/U$  is the volume integrated analog of the ratio  $P_{\text{kin}}/P_{\text{th}}$  and hence is also an indicator of formation history and substructure. We split our cluster sample equally into lower, middle and upper bands of  $K/U$  and define the sub-sample with the lowest ratio of  $K/U$  as *relaxed clusters*. We find that the clumping factor depends weakly on the dynamical state of the clusters. Overall, the relaxed clusters have a lower clumping factor in comparison to the entire sample. Figure 6 shows that for small radii ( $R \lesssim R_{200}$ ), the median clumping factor of relaxed clusters is below the 25<sup>th</sup> percentile of entire cluster sample. However, these differences between the relaxed and full cluster sample become progressively smaller outside the virial radius.

These trends can be understood by the fact that 1) clusters

of a given mass (range) show a larger degree of morphological disturbance/mass accretion at higher redshifts which probe on average dynamically younger objects and 2) the redshift evolution of the velocity anisotropy (cf. BBPS5) which shows that the average location of accretion shocks moves to smaller radii at larger  $z$  (if scaled by  $R_{200}$ , see Sec. 5 for more details). Hence at larger redshifts, also the gas distribution probes the infall/pre-accretion shock region that is shaped by the tides exerted by the far-field of clusters.

#### 4. CHARACTERIZING THE STRUCTURE OF CLUMPING

In the following, we aim at understanding the origin of the clumping, why there is a similar radial behavior of the density and pressure clumping, and to elucidate the relation of gas

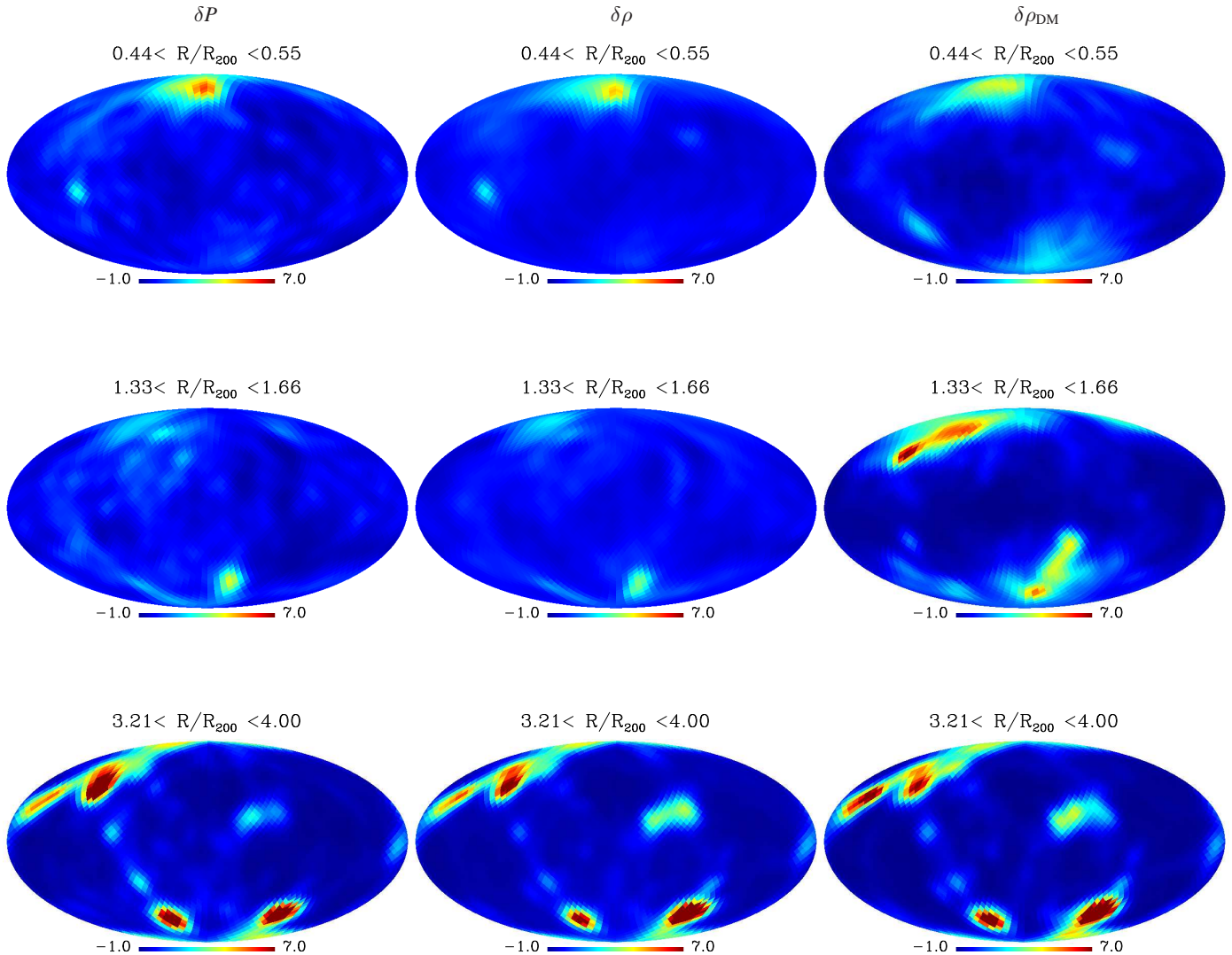


**Figure 7.** Mollweide equal area projections of the dimensionless fluctuations of the thermal pressure ( $\delta P$ , left panels), gas density ( $\delta\rho$ , middle panels), and DM density ( $\delta\rho_{\text{DM}}$ , right panels) for a cluster ( $M_{200} \simeq 1.15 \times 10^{15} M_{\odot}$ ,  $z = 0$ ) in radial shells at  $R \sim 0.5R_{200}$ ,  $R \sim 1.5R_{200}$ , and  $R \sim 4R_{200}$  (top to bottom). We project the fields onto 3072 angular pixels (using HEALPix with  $N_{\text{side}} = 16$ ) and smooth the maps to  $12^{\circ}$  FWHM. The color scale shows dimensionless fluctuations in linear units. Outside the virial radius, gas and pressure fluctuations show a strong correlation with the DM density, which becomes weaker for smaller radii due to dissipative gas effects in the ICM.

density and pressure to the underlying DM distribution. Following a similar procedure as described in BBPS3, we subdivide the gas density, pressure, and the DM density distributions into equal area angular cones. We use the HEALPix scheme (Górski et al. 2005), which uses equal area pixels on the sphere, with  $N_{\text{side}} = 16$  (3072 pixels). The value of  $N_{\text{side}}$  is a compromise between angular resolution and the rising contribution of the bin-to-bin variance due to SPH particle shot noise. In our treatment, SPH particles are projected using the SPH kernel in the radial direction but not in angular bins in order not to introduce an artificial smoothing of the power spectrum toward small angular scales, which is associated with the finite resolution.

#### 4.1. Projecting density and pressure fields onto the sphere

In Figures 7 and 8, we show Mollweide equal area projections of the gas density ( $\rho$ ), pressure ( $P$ ), and the DM density ( $\rho_{\text{DM}}$ ) for two massive, low-redshift clusters in three radial shells at  $R \sim 0.5R_{200}$ ,  $R \sim 1.5R_{200}$ , and  $R \sim 4R_{200}$ . We project the dimensionless fluctuations of the gas density ( $\delta\rho$ ), pressure ( $\delta P$ ), and the DM density ( $\delta\rho_{\text{DM}}$ ),

$$\begin{aligned} \delta\rho &= (\rho - \bar{\rho}) / \bar{\rho}, \\ \delta P &= (P - \bar{P}) / \bar{P}, \\ \delta\rho_{\text{DM}} &= (\rho_{\text{DM}} - \bar{\rho}_{\text{DM}}) / \bar{\rho}_{\text{DM}}. \end{aligned} \quad (10)$$

Here  $\bar{\rho}$ ,  $\bar{P}$ , and  $\bar{\rho}_{\text{DM}}$  are the mean values within each radial bin. We smooth the resulting maps to  $12^{\circ}$  full-width half-maximum (FWHM) for presentation purposes only. Our analysis is performed on the unsmoothed maps.

We also conducted the same analyses using the median in-

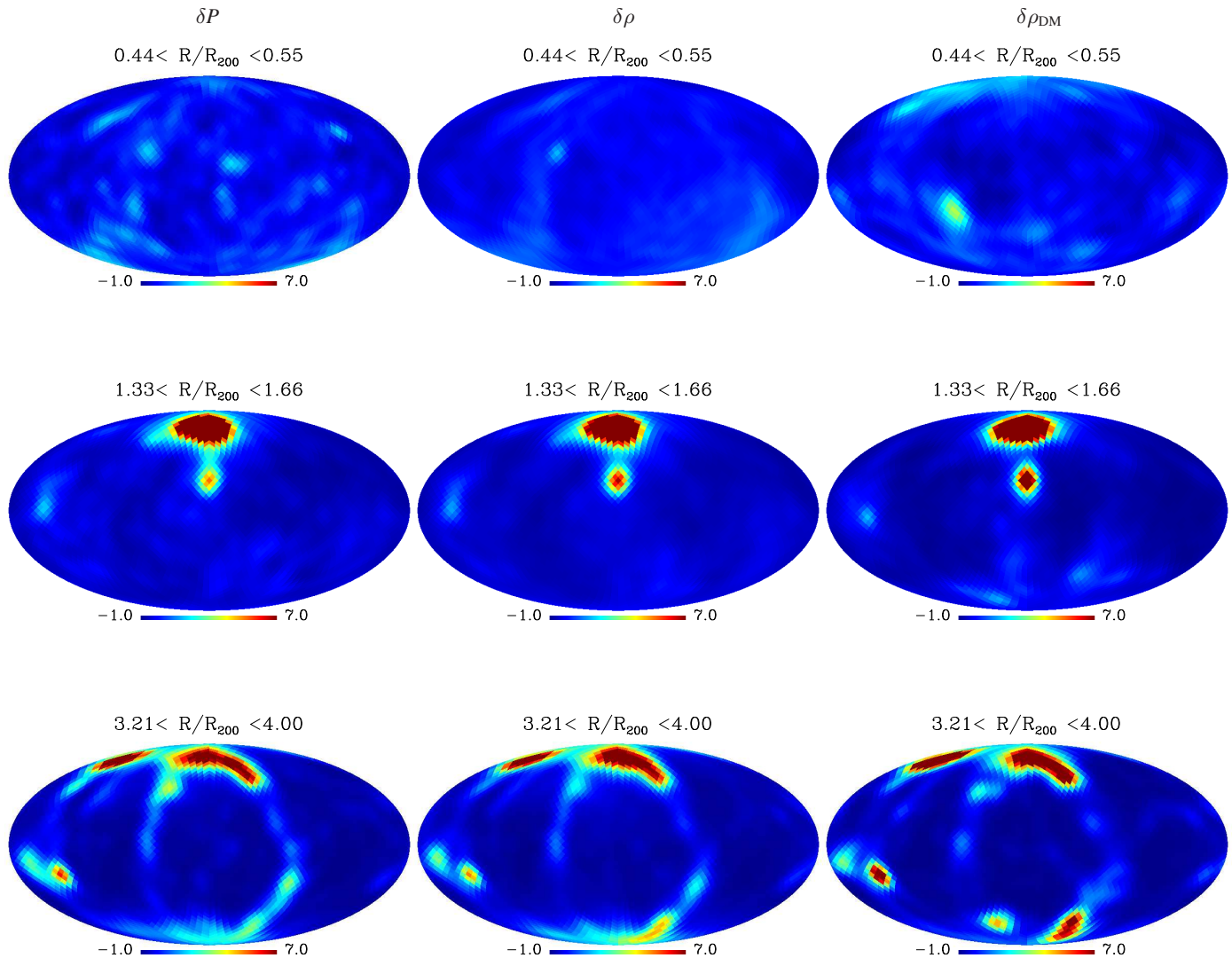


**Figure 8.** Same as Figure 7 for a  $M_{200} \simeq 6.5 \times 10^{14} M_{\odot}$  cluster at  $z=0$ .

stead of the mean for  $\bar{\rho}$ ,  $\bar{P}$ , and  $\bar{\rho}_{\text{DM}}$  and found very similar results. The construction of these fluctuating fields  $\delta\rho$ ,  $\delta P$ , and  $\delta\rho_{\text{DM}}$  is similar to subtracting the underlying smooth density and pressure profiles. However, by subtracting the mean in each radial bin we remove any residual radial, bin-to-bin correlations, which would have remained if we subtracted a best fit global profile. Lastly, when constructing these fields we adopted the same temperature cuts to  $\delta\rho$  as in Section 3.2, but not to  $\delta P$ .

Figures 7 and 8 illustrate that at a given radius (panels left to right) the gas density, pressure, and DM density are correlated. This correlation is stronger at  $R \sim 4R_{200}$  where the gas closely traces the DM structures while the correlation weakens for small radii ( $R \sim 0.5R_{200}$ ) because of dissipational gas effects in the ICM such as formation shocks and hydrodynamic instabilities. Comparing the maps at different radii, there is no apparent correlation between the small-scale fluctuations. In the following subsections we will quantify this.

The Mollweide projections and the observed trends do not

change for different physical simulation models. While global thermodynamic properties change upon varying the modeled physics (see, e.g., BBPS1), clumping and sub-structures remain almost invariant since they are related to halo growth, which is dominated by the gravitational potential. As a result, clumping factors and clump properties (such as sizes and shapes) are not affected by baryonic processes (e.g., Sec.3.3 and Roncarelli et al. 2013).

#### 4.2. Power-spectrum analysis

To quantify the angular structures in the projections shown in Figures 7 and 8, we perform an angular power-spectrum analysis of each un-smoothed dimensionless fluctuation field on the sphere. We use the *ANAFast* module in *HEALpix* that expands a projected field  $\delta$  into spherical harmonics,

$$\delta(\theta, \phi) = \sum_{\ell=0}^{\infty} \sum_{m=-\ell}^{\ell} a_{\ell,m} Y_{\ell}^m(\theta, \phi), \quad (11)$$

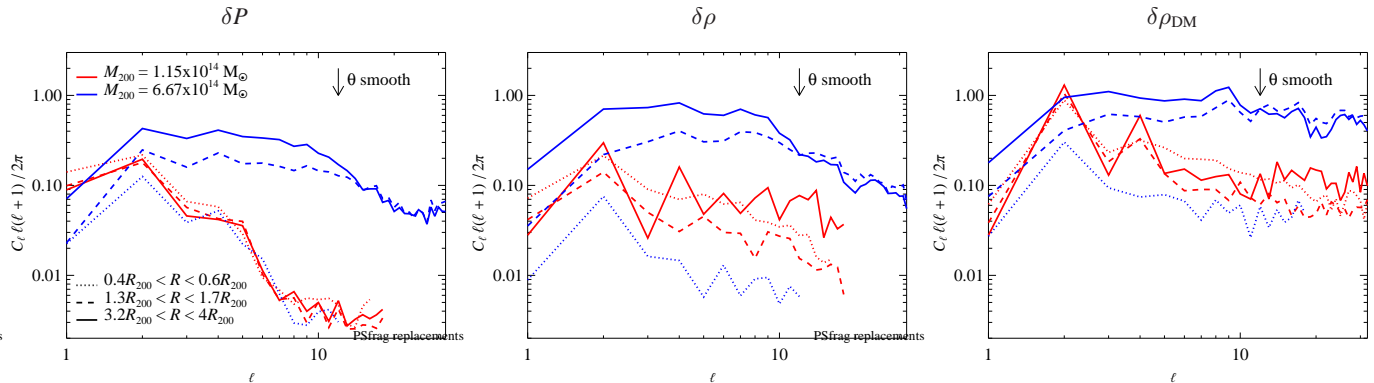


**Figure 9.** The angular power spectra ( $C_\ell$ ) of the dimensionless fluctuations of the thermal pressure ( $\delta P$ , left), gas density ( $\rho$ , middle), and DM density ( $\rho_{\text{DM}}$ , right) for the two clusters shown in Figures 7 (red lines) and 8 (blue lines) at  $R \sim 0.5R_{200}$ ,  $R \sim 1.5R_{200}$ , and  $R \sim 4R_{200}$ . In each panel, we indicate the smoothing scaling that was used in Figures 7 and 8 by an arrow. The large variations of  $C_\ell$  among those two clusters indicate the stochasticity introduced by the recent formation epoch of these systems.

$$a_{\ell,m} = \int d\Omega(\theta, \phi) \delta(\theta, \phi) Y_\ell^m(\theta, \phi). \quad (12)$$

Our analysis is analogous to that of quantifying the acoustic peaks in the cosmic microwave background with the exception that we obtain a different surface for each radial shell such that the physical scale of a given angular mode increases as the radius from the cluster center increases.

For a Gaussian field the statistics are completely described by the variance of the spherical harmonic eigenfunctions ( $a_{\ell,m}$ ). The projected fluctuation fields  $\delta\rho$ ,  $\delta P$ , and  $\delta\rho_{\text{DM}}$  each have non-Gaussian probability density functions so that there is additional information contained in their higher-order statistics. Here, we constrain ourselves to the analog of the two-point correlation in spherical harmonic space, the angular power spectrum. We calculate the angular auto spectra,

$$C_\ell = \frac{1}{2\ell+1} \sum_{m=-\ell}^{\ell} a_{\ell,m} a_{\ell,m}^*, \quad (13)$$

where the star denotes the complex conjugate, and the cross spectra,

$$C_\ell^{i,j} = \frac{1}{2\ell+1} \sum_{m=-\ell}^{\ell} a_{\ell,m}^i a_{\ell,m}^{j*} \quad (14)$$

for all radii and projected quantities  $i$  and  $j$ . We use the cross correlation coefficient,

$$r_{ij} = \frac{C_\ell^{i,j}}{\sqrt{C_\ell^{i,i} C_\ell^{j,j}}}, \quad (15)$$

to quantify the correlations between the different quantities and radii.

In Figure 9, we show the auto spectra of  $\delta\rho$ ,  $\delta P$ , and  $\delta\rho_{\text{DM}}$ , for the Mollweide projections of the two clusters shown in Figures 7 and 8. The large variations of  $C_\ell$  among those two clusters indicate the stochasticity introduced by the recent formation epoch of these systems, implying an incomplete relaxation for an “average” cluster. In all panels and at all radii the quadrupole ( $\ell = 2$  mode) dominates the normalized power spectrum, which shows that cluster ellipticity is an important source of clumping. Our results in BBPS1 demonstrate that clusters are predominately prolate over the range of radii shown, i.e., that the expansion coefficient of

$Y_2^2(\theta, \phi)$  carries most of the weight in the power-spectrum average.<sup>4</sup> However, the auto spectra show a broad spectrum of modes contributing to the signal and lack of prominent peaks beyond the quadrupole. Generally, the spectra of the outer radial shells show more power and are flatter than the spectra at smaller radii. This result is consistent with our findings in Section 3 (see also Nagai & Lau 2011; Zhuravleva et al. 2013; Roncarelli et al. 2013), which shows an increasing clumping factor at larger radii, particularly for  $\delta\rho_{\text{DM}}$ .

In Figure 10 we show the average auto power spectra for  $\delta\rho$ ,  $\delta P$ , and  $\delta\rho_{\text{DM}}$  at various radii. Here we averaged the spectra over massive clusters ( $5.1 \times 10^{14} M_\odot < M_{200} < 1.0 \times 10^{14} M_\odot$ ) and intermediate-mass clusters ( $2.6 \times 10^{14} M_\odot < M_{200} < 5.1 \times 10^{14} M_\odot$ ) at  $z = 0$ . We find that the average power spectra have similar features in comparison to the individual power spectra shown above. The spectra show a dominant quadrupole moment and the subsequent ringing in the even harmonics, albeit to a lesser extent. More massive cluster have more angular power than lighter clusters. However, the differences in angular power between different mass ranges is close to the cluster-to-cluster scatter.

The scaled angular power spectra of gas density and pressure show an evolution of the spectral shape from a broad bump at  $R_{200}/2$  to an almost flat distribution at  $4R_{200}$ . To understand which part of this evolution is driven by the decrease in angular larger when moving an object of fixed physical scale toward larger radii, we plot  $C_\ell$  as a function of  $(\ell+1/2)/x$ , where  $x = R/R_{200}$ , in Figure 11. In the small-angle limit,  $k_\perp = (\ell+1/2)/x$ , where  $k_\perp$  denotes the physical (perpendicular) wave number. The resulting power spectra of  $\delta P$  at different radii match very closely in shape while that of  $\delta\rho$  shows a residual offset with a slightly enhanced amplitude of  $C_\ell$  at larger radii. Most importantly, the gas density and pressure power spectra exhibit a broad bump, signaling the presence of “super-clumping” (McDonald et al. 2014). This demonstrates that gas density and pressure clumping are dominated by comparably large (sub-)structures with scales  $L_\perp \gtrsim \pi R_{200}/k_\perp \sim R_{200}/5$ , which do not get broken up through Kelvin-Helmholtz instabilities or transformed at shocks due to anisotropic stresses. We emphasize that this “super-clumping” is qualitatively different from possible signatures of “clumping” inferred in nearby clus-

<sup>4</sup> These auto spectra exhibit ringing features in the even harmonics, which signal an axis-symmetric mass distribution that cannot be fully described by an ellipsoidal shape and exhibits (sub-dominant) higher order contributions to the even harmonics.

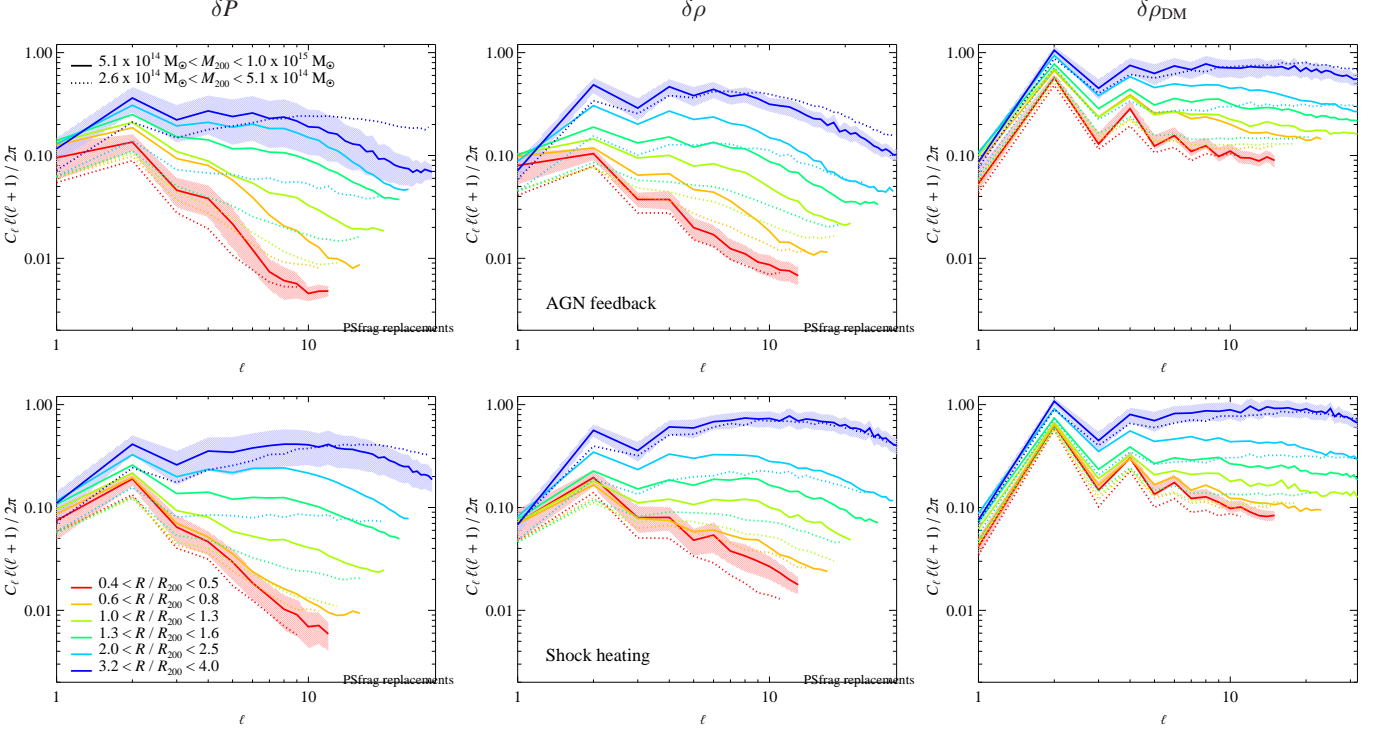


**Figure 10.** The average angular power spectra of the fluctuations in thermal pressure ( $P$ , left panels), gas density ( $\rho$ , middle panels), and the DM density ( $\rho_{\text{DM}}$ , right panels) at various radii (shown with different colors) for clusters within the mass ranges provided in the legend. The top panels show the power spectra of the AGN feedback simulations and the bottom panels show the shock heating-only simulations. Here the colored bands represent the error on the mean power spectrum for the smallest and largest radii, respectively. The quadrupole (mode with  $\ell = 2$ ) dominates the normalized power spectrum, which shows that cluster ellipticity is an important source of clumping. The general similarities between the average power spectra across the panels suggest that these spectra are largely independent of the simulated physics and cluster mass. The radial trend results from the different physical sizes associated with the angular scale at a given radius and changes in the background fields.

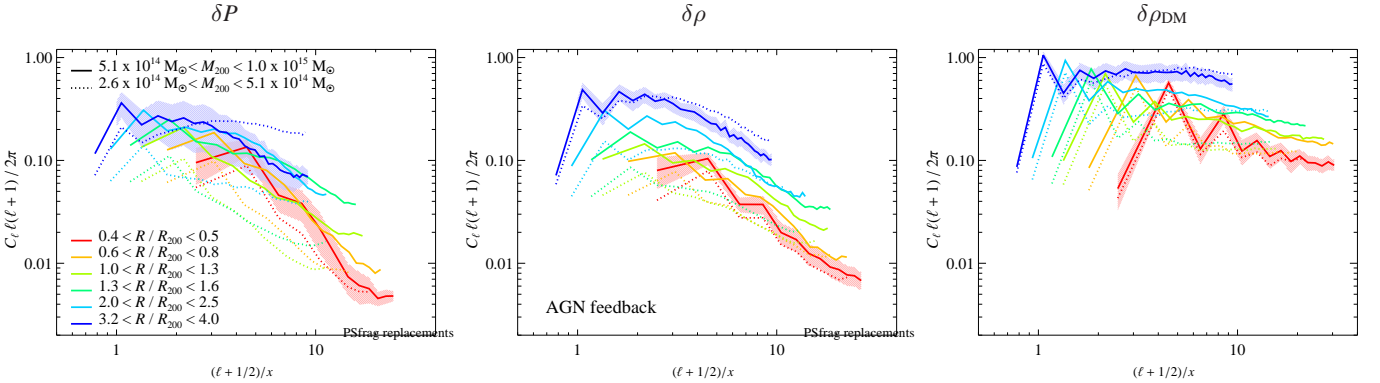


**Figure 11.** The average angular power spectra as a function of  $k_\perp \simeq (\ell+1/2)/x$ , where  $x = R/R_{200}$  (the equality sign in the equation for  $k_\perp$  assumes the small-angle limit). We show the fluctuations in thermal pressure ( $P$ , left), gas density ( $\rho$ , middle), and the DM density ( $\rho_{\text{DM}}$ , right) at various radii (shown with different colors) for clusters within the mass ranges provided in the legend. Here the colored bands represent the error on the mean power spectrum for the smallest and largest radii, respectively. After scaling the abscissa to the same physical scale, the gas density and pressure power spectra at different radii delineate the same spectral bump (albeit with different spatial resolution), indicating the presence of “super-clumping”. In contrast, the DM density power spectrum remains comparably flat toward smaller scales, which implies a continuous distribution of subhalos.

ters (e.g., Simionescu et al. 2011; Urban et al. 2014), which has been interpreted as a distribution of subhalos accreting onto clusters, whereas group-sized halos would be directly detected and masked.

In contrast, the angular power spectrum of the DM density (right panel, Figure 11) shows an almost uniform size distribution (at radii  $> R_{200}/2$ ) due to subhalos within clusters that are not subject to hydrodynamic forces. We note that tidal effects are only expected to modify the DM substructure distribution at smaller radii (Gao et al. 2012). The auto power spec-

trum of  $\delta \rho_{\text{DM}}$  has the largest amplitude among the three fields, since the DM only interacts gravitationally whereas gas additionally feels the hydrodynamic force. This force leads to transient phenomena such as shocks, contact discontinuities, and hydrodynamic instabilities, which effectively smooth the gas density and pressure distributions. This results in smaller contrasts across the sky and less power. Among the three fields, the pressure shows the smallest amplitude of the auto power spectrum. While contact discontinuities have density jumps across, which are in part responsible for the angular power, the

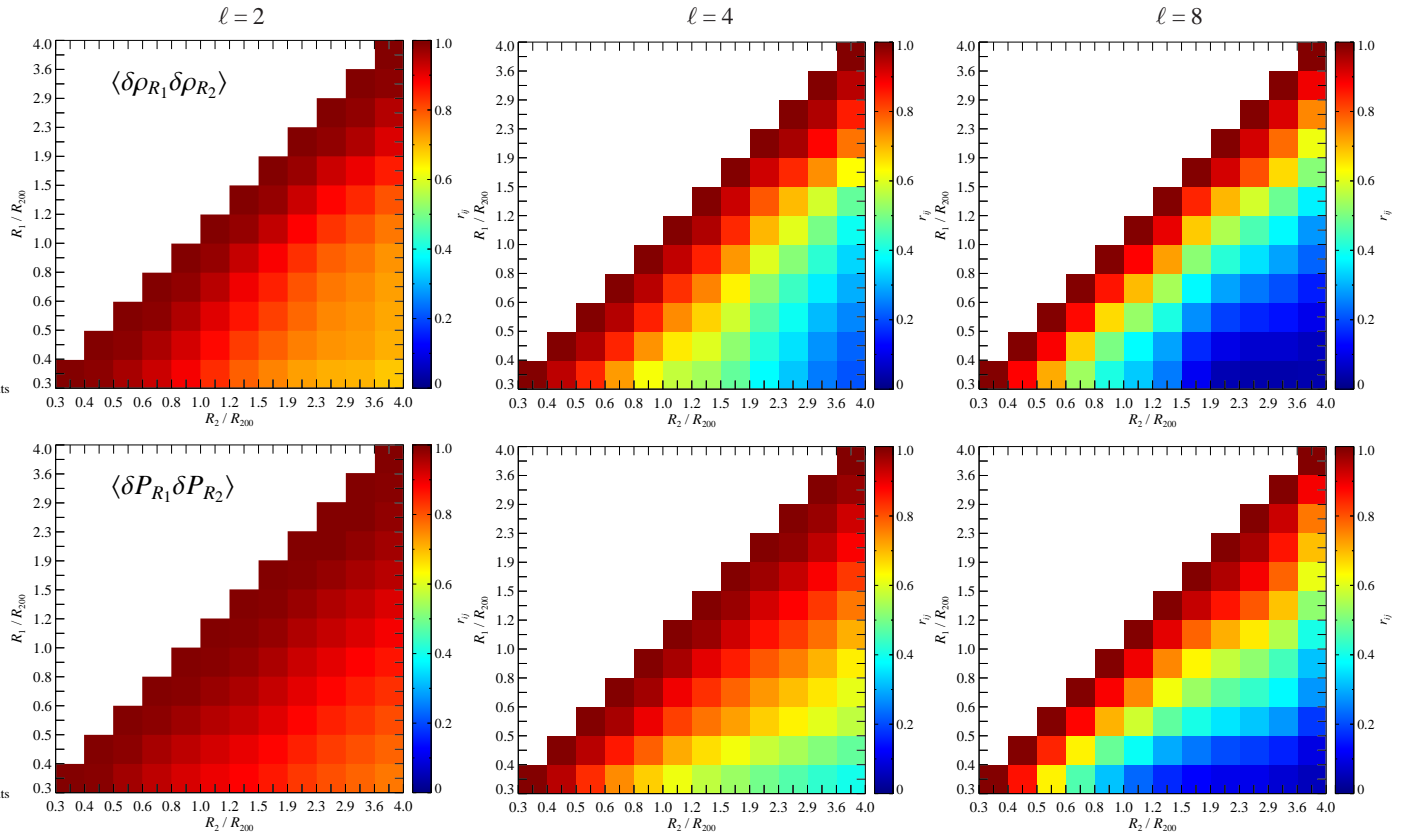


**Figure 12.** Matrix of the average radial cross correlation for clusters with masses  $5.1 \times 10^{14} M_{\odot} < M_{200} < 1 \times 10^{15} M_{\odot}$  at a given multipole moment ( $\ell$ ) that scales inversely with angular scale. From the top to bottom, we show the radial cross correlation of gas density ( $\langle \delta\rho_{R_1} \delta\rho_{R_2} \rangle$ ) and pressure ( $\langle \delta P_{R_1} \delta P_{R_2} \rangle$ ) at different multipoles  $\ell = 2, 4$ , and  $8$  (left to right). The color scale ranges from red (highly correlated) to blue (uncorrelated). From the inner to the outer radii the  $\ell = 2$  mode is highly correlated, so the quadrupole moment at the inner radii correlates with the moment at the outer radii. This radial cross correlation does not hold for a large radial range for higher multipole moments and becomes successively weaker as  $\ell$  increases.

pressure is constant across contact discontinuities. Hence, the pressure field exhibits less discontinuities and appears generally smoother which causes a smaller angular power. There is indirect evidence for such an interpretation of our findings from X-ray observations of the ICM. These find abundant “cold fronts”, which are identified with sloshing contact discontinuities (e.g., Markevitch & Vikhlinin 2007; ZuHone et al. 2010, and references therein).

The power spectrum amplitude increases with radius. This is in line with our findings for the clumping factor and expected since the background pressure and density distributions (gas and DM) are decreasing with radius. Thus, clumps of similar amplitude have a greater contrast with these backgrounds at larger radii. Power spectra are measurements of variances, so a larger contrast with the background implies a greater power spectrum amplitude.

As shown in Figure 10, there are no significant differences of the mean angular power spectra between the various simulated physics models. This result is similar to the results found in Section 3 and furthermore confirms that clumping in our simulations is mainly due to gravitationally dominated processes, which are only modulated by baryonic physics.

When we discretise the distributions of gas mass and thermal energy into individual cones, we use the SPH kernel in the radial direction but not for projection into angular pixels in order not to introduce an artificial smoothing that is associated with the finite resolution. If we had distributed the fraction of SPH mass and energy within the smoothing kernel that is

subtended by the solid angle of the HEALPix cone, this would have caused an artificial decrease of the amplitude of the power spectrum toward small scales, which scales as the square of the Fourier transform of the SPH smoothing kernel and reveals the inability to resolve structures on scales below the smoothing kernel. Instead, we decided to cut the power spectra at the multipole moment  $\ell_{\max}$  at which the SPH particle shot noise term dominates the power, thereby demarcating their angular resolution. The particle shot noise is smaller for more massive clusters and at larger radii, implying an increasing  $\ell_{\max}$  with cluster mass and radius. This can be understood with a simple analytical model that relates the solid angle subtended by the SPH particle’s smoothing radius to the cluster centric radius of that particle, yielding

$$\ell_{\max} \simeq \frac{\pi}{\theta_{\max}} = \left( \frac{\pi^3 x^3 \rho \sqrt{C_{2,\rho}} M_{200}}{200 \rho_{\text{cr}} N_{\text{gas}} m_{\text{gas}}} \right)^{1/3}, \quad (16)$$

where  $x = R/R_{200}$  and  $\rho_{\text{cr}}$  is the critical mass density of the universe. Note that the inclusion of the density clumping factor ( $C_{2,\rho}$ ) is important to account for the increase of  $\ell_{\max}$  at radii much larger than the scale radius of the density profiles.

#### 4.3. Cross-power spectra

We calculate the cross correlation coefficient ( $r_{ij}$ , cf. Equation (15)) for projected quantities between different radial shells as well as between projected quantities. Values of  $r_{ij}$  close to unity imply strongly correlated quantities and those

close to zero show that the quantities are uncorrelated.

In Figures 12 and 13 we show multiple panels of cross correlation coefficients  $r_{ij}$  between different radial bins for a fixed angular scale. We present  $r_{ij}$  as a matrix for a given multipole moment  $\ell$  that is symmetric if we cross correlate a quantity with itself. In the latter case, i.e., when we cross correlate  $\delta\rho$  with  $\delta P$  or  $\delta\rho_{\text{DM}}$  as a function of radial separation, then the diagonal corresponds to the cross correlation amplitude at that radius, which we show as a function of  $\ell$  in left panel of Figure 14.

For the quadrupole moment ( $\ell = 2$ ), we find cross correlation coefficients very close to unity for all radial correlations of  $\delta\rho$ ,  $\delta P$ ,  $\delta\rho \times \delta P$  and  $\delta\rho \times \delta\rho_{\text{DM}}$ . Thus, the orientation of the gas and pressure ellipticities in the inner regions of clusters are spatially aligned with the outer regions (BBPS1). We show that density and pressure enhancements correlate along the cones for small  $\ell$  (i.e., on large angular scales). This suggests that cosmological filaments, which connect to clusters, have a large influence on the cluster's quadrupole moment deep into the cluster interior and that clumping is in part due to substructure that is infalling along filaments into cluster cores. Therefore, the direction of the most over-dense cones will coincide with the direction of the major axis of the moment-of-inertia tensor.

The higher angular moments  $\ell = 4$  and 8 show less correlation between radial shells. However, radial shells beyond the virial radius show a stronger correlation to shells that are further apart in comparison to scales within the cluster that lose coherence to adjacent radial shells. For  $\ell = 4$  the correlation is still strong for radial bins that are  $\sim 3-4$  bins away. This coherence drops to adjacent bins when we look at  $\ell = 8$ . Overall the correlations are weaker for the gas density than for the pressure.

We find that inter-quantity cross correlations are generally weaker in comparison to the cross correlations of a quantity with itself. With increasing multipole moments, the correlations are confined to successively smaller radial ranges at any radius. For multipole moments  $\ell \geq 4$ , the inter-quantity correlations is weak at large radii and becomes uncorrelated inside of  $R/R_{200} \sim 1.5$ , which coincides with the approximate location of the virial shock.

In Figure 14 we show the radial cross correlation of  $\delta\rho$  with  $\delta P$  and with  $\delta\rho_{\text{DM}}$  as a function of  $\ell$ . As we increase the separation between the radial shells, the correlations between the gas density and pressure decreases. The same happens with the correlation between gas and DM density. Thus, the gas at small radius has lost the memory of its previous state before infall, when it more closely correlated to DM. Not surprisingly this is the result of dissipational virialization. However, this loss of information is not instantaneous since the intermediate radial bins are still marginally correlated with the inner most radial bin.

## 5. THE PHYSICS OF CLUSTER OUTSKIRTS

We now attempt a comprehensive view of the physics of cluster outskirts and provide a synopsis of various non-equilibrium measures that all become increasingly important beyond  $R_{200}$ . Those include the kinetic pressure support of the gas (see Equation (8)), the gas ellipticity (characterized by the axis ratio of the moment-of-inertia tensor), density and pressure clumping as a function of cluster radius. First we review the definition of ellipticity (for further details, please refer to BBPS1).

We estimate the deviation from spherical symmetry of the cluster gas and dark matter distribution through the moment-

of-inertia tensor,

$$I_{ij}(r < R) = \frac{\sum_{\alpha} m_{\alpha} (x_{i,\alpha} - \bar{x})(x_{j,\alpha} - \bar{x})}{\sum_{\alpha} m_{\alpha}}, \quad (17)$$

where  $\alpha$  labels all particles within a given radius  $R$ ,  $x_i$  is the  $i$ th coordinate of particle  $\alpha$ , and  $m$  is its mass. We quantify the ellipticity of cluster gas and DM density using the eigenvalues  $\lambda_i$ , which are computed for each inertial tensor at a given radius. We adopt the convention  $\lambda_1 < \lambda_2 < \lambda_3$  for the eigenvalues. The ellipsoid associated with the tensor has half-axis lengths  $a = \sqrt{\lambda_1}$ ,  $b = \sqrt{\lambda_2}$ , and  $c = \sqrt{\lambda_3}$ .

In Figure 15, we show the radial profiles of the kinetic-to-thermal pressure ratio  $P_{\text{kin}}/P_{\text{th}}$ , the axis ratio of the moment-of-inertia tensor  $1 - c/a$ , and the density and pressure clumping factors (corrected for SPH volume bias). Inside  $R_{200}$ , all these dissipative non-equilibrium statistics show fairly small values, which increase dramatically for  $R \gtrsim R_{200}$  (within a radial range of a factor of 2). At any radius, heavier clusters and/or clusters at higher redshift show an increased level of these non-equilibrium statistics since these probe on average dynamically younger objects.

Starting from the inside out, we encounter first a rising ratio of  $P_{\text{kin}}/P_{\text{th}}$ , followed by density and pressure clumping, and last by the gas ellipticities. Those different transition radii provide evidence for the different timescales on which these non-equilibrium statistics approach sphericalization/virialization as structures get accreted by a cluster, transforms into substructures, and eventually resolve within the ICM.

The smooth transition of the kinetic-to-thermal pressure ratio demonstrates that cluster accretion shocks do not thermalize all kinetic energy immediately. Instead the curvature of their shock surfaces induces vorticity (Pfrommer & Jones 2011) which drives a turbulent cascade that dissipates the energy contained within a few eddy-turnover times in the comoving frame of the accreting gas (Shi & Komatsu 2014).

In contrast, these post-shock shear flows destroy the peripheral parts of accreted substructures on a faster time scale through Kelvin-Helmholtz instabilities, causing the density and pressure clumping factors to drop shortly after the accretion shocks, the location of which apparently moves in as a function of redshift in our radial representation  $R/R_{200}$ . However, as we show in BBPS1 (and later on confirmed by Nelson et al. (2014)), this is an artifact of the definition of the virial radius  $R_{200}$  (of taking a sphere enclosing a mean density that is 200 times the *critical* density of the universe) and almost stays fixed when changing the definition to  $R_{200m}$  (i.e., evaluating the mean density within a sphere that is 200 times the *mean* density of the universe).

Finally, the gas ellipticities show the transition to a smaller value at the largest radius, as this statistic responds to the overall potential shape that has been established through accretion along a few filaments connecting to the cluster from different angular directions. Contrarily, the dissipationless DM component shows an elevated level of ellipticity with only modest decline towards smaller radii, presumably owing to gravitational exchange with the dissipational gas component.

## 6. CONCLUSIONS

Quantifying and characterizing density and pressure clumping is essential for eliminating observational biases in determining various ICM properties. In X-ray measurements, density clumping will bias the estimates of the ICM density, which has observational consequences such as an apparent flattening

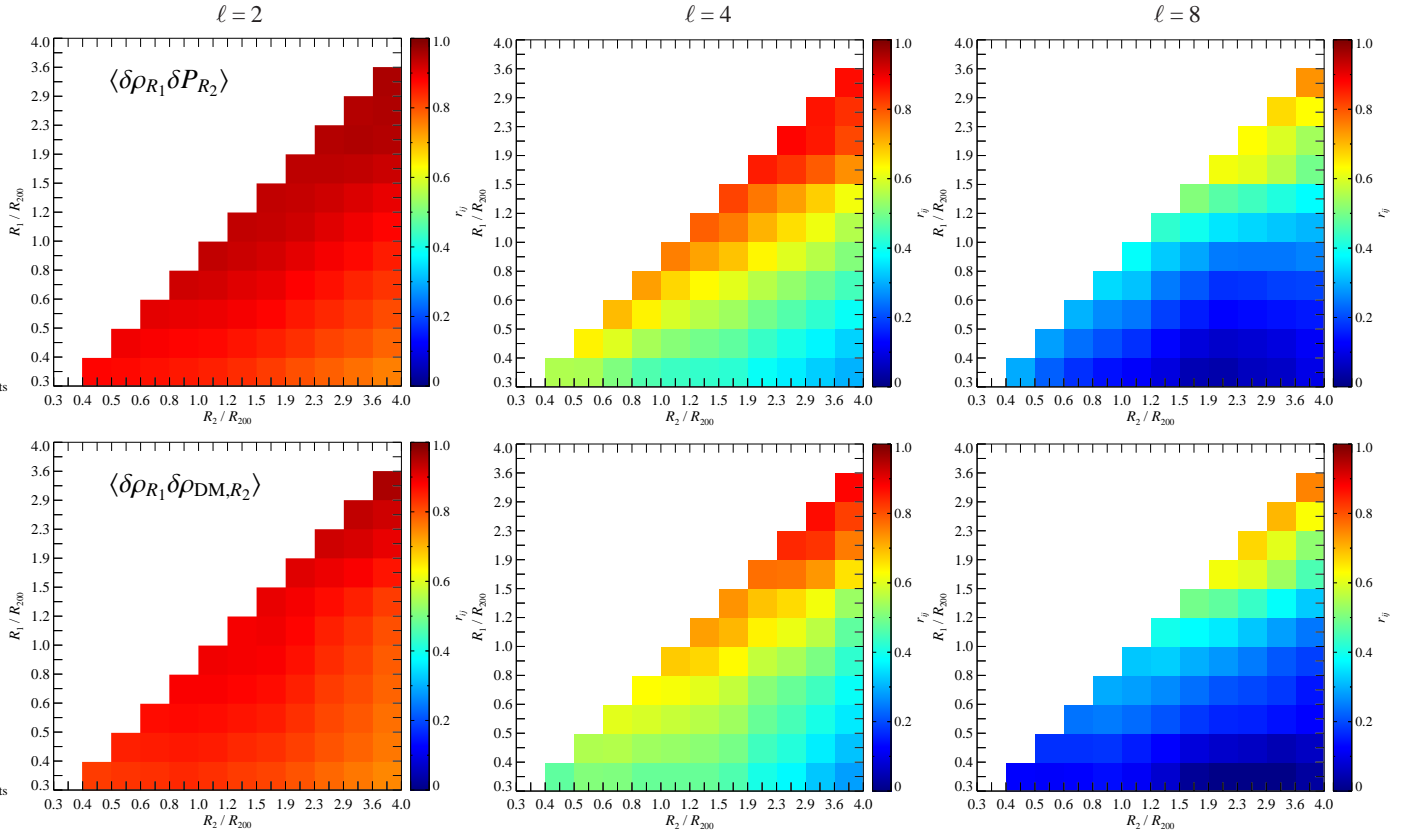


**Figure 13.** Same as in Figure 12, but for the radial cross correlation of  $\rho$  and  $P$  ( $\langle \delta\rho_{R_1} \delta P_{R_2} \rangle$ , top) and  $\rho$  and  $\rho_{\text{DM}}$  ( $\langle \delta\rho_{R_1} \delta\rho_{\text{DM},R_2} \rangle$ , bottom). With increasing multipole moments, the correlations are confined to successively smaller radial ranges. These inter-quantity cross correlations are generally weaker in comparison to the cross correlations of a quantity with itself (cf. Figure 12).

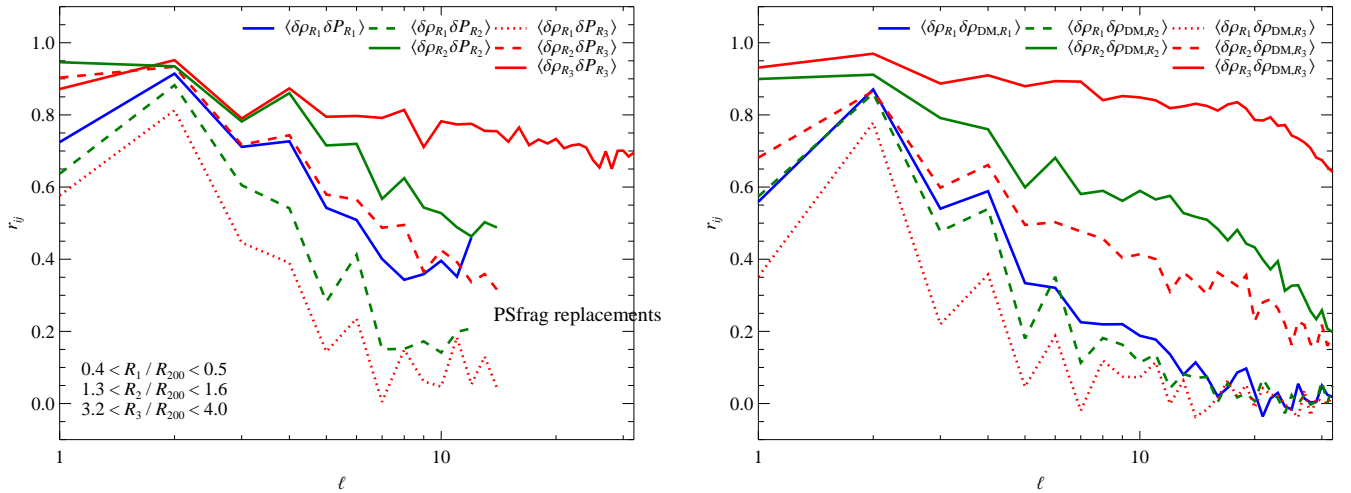


**Figure 14.** Average radial cross correlation coefficient of  $\delta\rho$  with  $\delta P$  (left) and with  $\delta\rho_{\text{DM}}$  (right) for clusters with masses  $5.1 \times 10^{14} M_{\odot} < M_{200} < 1 \times 10^{15} M_{\odot}$  as a function of multipole moment  $\ell$ . The correlation coefficient decreases for cluster-centric shells that are further apart and for smaller angular scales (as  $\ell$  increases). For the greatest shell separation (red dotted lines) there is no correlation beyond  $\ell \gtrsim 6$ . Gas that is accreted onto clusters passes through the cluster accretion shock, which heats it to the clusters' virial temperature and starts to separate it from the DM halo that does not feel the pressure force.

in the entropy profile and apparent baryon fractions that exceed the cosmic mean. The consequence of pressure clumping are more subtle in comparison to density clumping. Variations about mean pressure profiles will increase the amplitude of the thermal SZ auto spectrum as a function of  $\ell$  and increase the scatter in the  $Y - M_{200}$  scaling relation.

To address these biases, we presented an analysis of ICM inhomogeneities (clumping) using cosmological hydrodynamic simulations with different variants of subgrid physics included. Our analysis can be categorized into two approaches: (1) quantifying the so-called *clumping factor* (i.e., the dimensionless second-order moment of density or pressure) as a function of radius and (2) characterizing the angular structure of these inhomogeneities with the goal of understanding its nature. Our results can be summarized as follows.

- Similar to the previous work (e.g., Nagai & Lau 2011; Roncarelli et al. 2013) we find that the clumping factor increases with radius and is independent of the sub-grid physics model used (see Figures 2 and 4). This indicates that the process giving rise to clumping is gravitational in nature and only modulated by baryonic physics. However, our AGN feedback model at higher redshifts ( $z \gtrsim 1$ ) shows a moderate suppression of clumping outside  $R_{200}$  due to the smoothing effect of the feedback energy.
- Density and pressure clumping are increasing functions of cluster mass and redshift (see Figures 5 and 6), which probe on average dynamically younger objects that are still in the process of assembling. Hence this is a consequence of hierarchical structure growth.
- We find a small trend with the dynamical state of a cluster, with relaxed clusters exhibiting lower clumping factors for both density and pressure (see Figure 6). However, the differences are within the 25<sup>th</sup> and 75<sup>th</sup> percentiles of the distributions of clumping factors.
- The inhomogeneities that are responsible for density and pressure clumping can be clearly identified in the angular projections of radial shells (see Figures 7 and 8 for examples of a massive and intermediate-mass cluster). The angular power spectra of these inhomogeneities have a prominent quadrupole feature and increase with amplitude as the spatially smoothed background field decreases (see Figure 10).
- When the angular power spectra of gas density and pressure are plotted as a function of physical (perpendicular) wavenumber, they show a universal broad peak at large scales (see Figure 11), signaling the presence of gravitationally-driven “super-clumping” (McDonald et al. 2014). Hence, the gas density and pressure clumping signal is dominated by comparably large substructures with scales  $\gtrsim R_{200}/5$ . Smaller structures apparently get broken up through Kelvin-Helmholtz instabilities or are transformed at shocks due to anisotropic stresses. In contrast, the angular power spectrum of the DM density shows an almost uniform size distribution at all radii due to unimpeded distributions of subhalos within clusters (see Figure 11), which are not subject to hydrodynamic forces nor are they affected by tidal effects at cluster-centric radii  $> R_{200}/3$ .
- The quadrupole correlates across all radial shells (for radii  $> R_{200}/3$ ), indicating that the direction of clumping is determined by infalling substructures into clusters (see Figure 12). At smaller angular scales (for multipole moments  $\ell \geq 4$ ), the cross correlation becomes weaker with increasing radial distance between the two shells, in particular for smaller radii and when we correlate different quantities such as gas density and pressure (see Figure 13).
- Combining our results from clumping, angular power spectra, and cross correlation coefficients, we find that these inhomogeneities are sourced by cosmic filaments that are channeling baryonic and dark matter onto clusters.
- We finally provide a synopsis of the clusters’ non-equilibrium and non-spherical measures such as kinetic pressure support of the gas, gas ellipticity (characterized by the axis ratio of the moment-of-inertia tensor), density and pressure clumping as a function of cluster radius. All these measures increase sharply beyond  $R_{200}$  (see Figure 15).

We thank Chris Thompson for useful discussions. Research in Canada is supported by NSERC and CIFAR. Simulations were run on SCINET and CITA’s Sunnyvale high-performance computing clusters. SCINET is funded and supported by CFI, NSERC, Ontario, ORF-RE and UofT deans. C.P. gratefully acknowledges financial support of the Klaus Tschira Foundation. We also thank KITP for their hospitality during the 2011 galaxy cluster workshop. KITP is supported by National Science Foundation under Grant No. NSF PHY05-51164.

## REFERENCES

- Ackermann, M. et al. 2013, ArXiv:1308.5654  
Akamatsu, H., Hoshino, A., Ishisaki, Y., Ohashi, T., Sato, K., Takei, Y., & Ota, N. 2011, PASJ, 63, 1019  
Aleksić, J. et al. 2012, A&A, 541, A99  
Allen, S. W., Rapetti, D. A., Schmidt, R. W., Ebeling, H., Morris, R. G., & Fabian, A. C. 2008, MNRAS, 383, 879  
Arlen, T. et al. 2012, ApJ, 757, 123  
Arnaud, M., Pratt, G. W., Piffaretti, R., Böhringer, H., Croston, J. H., & Pointecouteau, E. 2010, A&A, 517, A92  
Avestruz, C., Lau, E. T., Nagai, D., & Vikhlinin, A. 2014, ArXiv:1404.4634  
Bardeen, J. M., Bond, J. R., Kaiser, N., & Szalay, A. S. 1986, ApJ, 304, 15  
Battaglia, N., Bond, J. R., Pfrommer, C., & Sievers, J. L. 2012a, ApJ, 758, 74  
—. 2012b, ApJ, 758, 75  
—. 2013, ApJ, 777, 123  
—. 2014, in prep.  
Battaglia, N., Bond, J. R., Pfrommer, C., Sievers, J. L., & Sijacki, D. 2010, ApJ, 725, 91  
Bautz, M. W. et al. 2009, PASJ, 61, 1117  
Bond, J. R., & Myers, S. T. 1996, ApJS, 103, 1  
Carlstrom, J. E. et al. 2011, PASP, 123, 568  
Churazov, E. et al. 2012, MNRAS, 421, 1123  
Eckert, D., Ettori, S., Molendi, S., Vazza, F., Roncarelli, M., Gastaldello, F., & Rossetti, M. 2013, ArXiv:1310.8389  
Enßlin, T. A., Pfrommer, C., Springel, V., & Jubelgas, M. 2007, A&A, 473, 41  
Evrard, A. E. 1990, ApJ, 363, 349  
Fabian, A. C. et al. 2011, MNRAS, 418, 2154  
Fowler, J. W. et al. 2007, Appl. Opt., 46, 3444  
Gao, L., Navarro, J. F., Frenk, C. S., Jenkins, A., Springel, V., & White, S. D. M. 2012, MNRAS, 425, 2169  
George, M. R., Fabian, A. C., Sanders, J. S., Young, A. J., & Russell, H. R. 2009, MNRAS, 395, 657  
Górski, K. M., Hivon, E., Banday, A. J., Wandelt, B. D., Hansen, F. K., Reinecke, M., & Bartelmann, M. 2005, ApJ, 622, 759

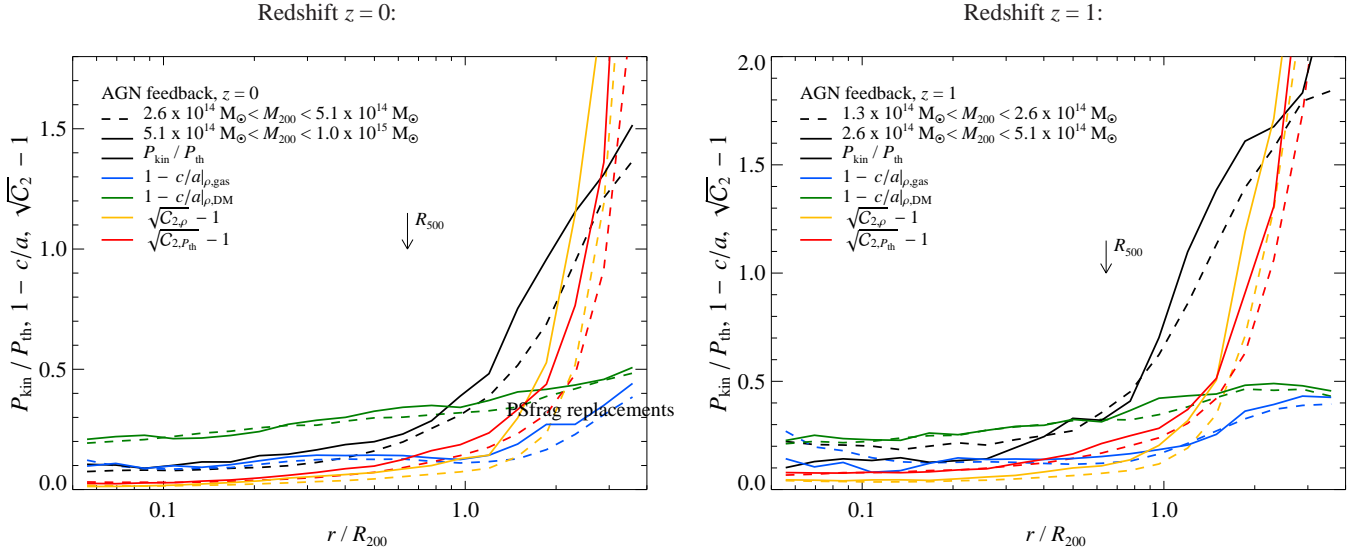


**Figure 15.** The outskirts of clusters become increasingly complicated since traditionally simplifying assumptions dramatically break down around and beyond the virial radius. This is demonstrated by comparing the median profiles of the non-thermal pressure contribution,  $P_{\text{kin}}/P_{\text{th}}$ , the asphericity estimate for DM and gas,  $1-c/a$  (where  $c/a$  is the ratio of the largest-to-smallest main axis of the moment-of-inertia tensor), as well as gas density and pressure clumping factor,  $C_2$ , which all increase dramatically with radius. We contrast low- and high-mass clusters (dashed and solid) at  $z=0$  (left) and  $z=1$  (right). Note the different range of the ordinate values in both panels. Those simplifying assumptions break down more significantly for larger clusters (at the same  $z$ ) and earlier times (i.e., larger  $z$  for fixed cluster mass) since both criteria probe on average dynamically younger objects in a hierarchically growing universe.

Hajian, A., Battaglia, N., Spergel, D. N., Bond, J. R., Pfrommer, C., & Sievers, J. L. 2013, JCAP, 11, 64  
Hasselfield, M. et al. 2013, JCAP, 7, 8  
Hoshino, A. et al. 2010, PASJ, 62, 371  
Jubelgas, M., Springel, V., Enßlin, T., & Pfrommer, C. 2008, A&A, 481, 33  
Kasun, S. F., & Evrard, A. E. 2005, ApJ, 629, 781  
Kawaharada, M. et al. 2010, ApJ, 714, 423  
Khedekar, S., Churazov, E., Kravtsov, A., Zhuravleva, I., Lau, E. T., Nagai, D., & Sunyaev, R. 2013, MNRAS, 431, 954  
Lau, E. T., Kravtsov, A. V., & Nagai, D. 2009, ApJ, 705, 1129  
Lau, E. T., Nagai, D., Kravtsov, A. V., & Zentner, A. R. 2011, ApJ, 734, 93  
Macciò, A. V., Dutton, A. A., & van den Bosch, F. C. 2008, MNRAS, 391, 1940  
Mantz, A., Allen, S. W., Rapetti, D., & Ebeling, H. 2010, MNRAS, 406, 1759  
Mantz, A. B., Allen, S. W., Morris, R. G., Rapetti, D. A., Applegate, D. E., Kelly, P. L., von der Linden, A., & Schmidt, R. W. 2014, MNRAS, 440, 2077  
Markevitch, M., & Vikhlinin, A. 2007, Phys. Rep., 443, 1  
McDonald, M. et al. 2014, ArXiv:1404.6250  
McNamara, B. R., & Nulsen, P. E. J. 2007, ARA&A, 45, 117  
Mohr, J. J., Fabricant, D. G., & Geller, M. J. 1993, ApJ, 413, 492  
Morandi, A., & Cui, W. 2014, MNRAS, 437, 1909  
Nagai, D., & Lau, E. T. 2011, ApJ, 731, L10  
Nelson, K., Lau, E. T., & Nagai, D. 2014, ArXiv:1404.4636  
Nelson, K., Rudd, D. H., Shaw, L., & Nagai, D. 2012, ApJ, 751, 121  
Pfrommer, C., Enßlin, T. A., Springel, V., Jubelgas, M., & Dolag, K. 2007, MNRAS, 378, 385  
Pfrommer, C., & Jones, T. W. 2011, ApJ, 730, 22  
Pfrommer, C., Springel, V., Enßlin, T. A., & Jubelgas, M. 2006, MNRAS, 367, 113  
Planck Collaboration et al. 2013a, ArXiv:1303.5080  
—. 2013b, ArXiv:1303.5081

—. 2013c, A&A, 550, A131  
—. 2011a, A&A, 536, A8  
—. 2011b, A&A, 536, A11  
—. 2011c, A&A, 536, A12  
—. 2011d, A&A, 536, A10  
Rasia, E., Tormen, G., & Moscardini, L. 2004, MNRAS, 351, 237  
Reichardt, C. L. et al. 2012, ApJ, 755, 70  
—. 2013, ApJ, 763, 127  
Reiprich, T. H. et al. 2009, A&A, 501, 899  
Roncarelli, M., Ettori, S., Borgani, S., Dolag, K., Fabjan, D., & Moscardini, L. 2013, MNRAS, 432, 3030  
Roncarelli, M., Ettori, S., Dolag, K., Moscardini, L., Borgani, S., & Murante, G. 2006, MNRAS, 373, 1339  
Sato, T. et al. 2012, ArXiv:1203.1700  
Shi, X., & Komatsu, E. 2014, ArXiv:1401.7657  
Sievers, J. L. et al. 2013, JCAP, 10, 60  
Simionescu, A. et al. 2011, Science, 331, 1576  
Springel, V. 2005, MNRAS, 364, 1105  
Springel, V., & Hernquist, L. 2003, MNRAS, 339, 289  
Sunyaev, R. A., & Zeldovich, Y. B. 1970, Ap&SS, 7, 3  
Thompson, T. A., Quataert, E., & Murray, N. 2005, ApJ, 630, 167  
Urban, O. et al. 2014, MNRAS, 437, 3939  
Vazza, F., Brunetti, G., Kritsuk, A., Wagner, R., Gheller, C., & Norman, M. 2009, A&A, 504, 33  
Vazza, F., Eckert, D., Simionescu, A., Brügggen, M., & Ettori, S. 2013, MNRAS, 429, 799  
Vikhlinin, A. et al. 2009, ApJ, 692, 1060  
Walker, S. A., Fabian, A. C., Sanders, J. S., George, M. R., & Tawara, Y. 2012, ArXiv:1203.0486  
Zhuravleva, I., Churazov, E., Kravtsov, A., Lau, E. T., Nagai, D., & Sunyaev, R. 2013, MNRAS, 428, 3274  
ZuHone, J. A., Markevitch, M., & Johnson, R. E. 2010, ApJ, 717, 908

## APPENDIX

### A. INSIGHTS INTO CORRECTIONS FOR SPH VOLUME BIAS

In Figure 16, we demonstrate how SPH volume correction affect the density moments (to second order and to first negative order). For the latter case, the SPH volume bias correction removes unphysical density moment estimates smaller than unity. The temperature cut in radiative simulations (i.e., considering only SPH particles with  $T > 10^6$  K) is only im-

portant for positive density moments (see Figure 3), which are biased by dense gas clumps.

The influence of a temperature cut is negligible for zeroth or  $n$ th order negative density moments that intentionally down-weight the dense and cold clumps. This is explicitly shown in Figure 1 demonstrating that the SPH volume bias is almost independent of the simulated physics. In contrast, applying a temperature cut to  $\tilde{C}_0$  or  $n$ th order negative density moments

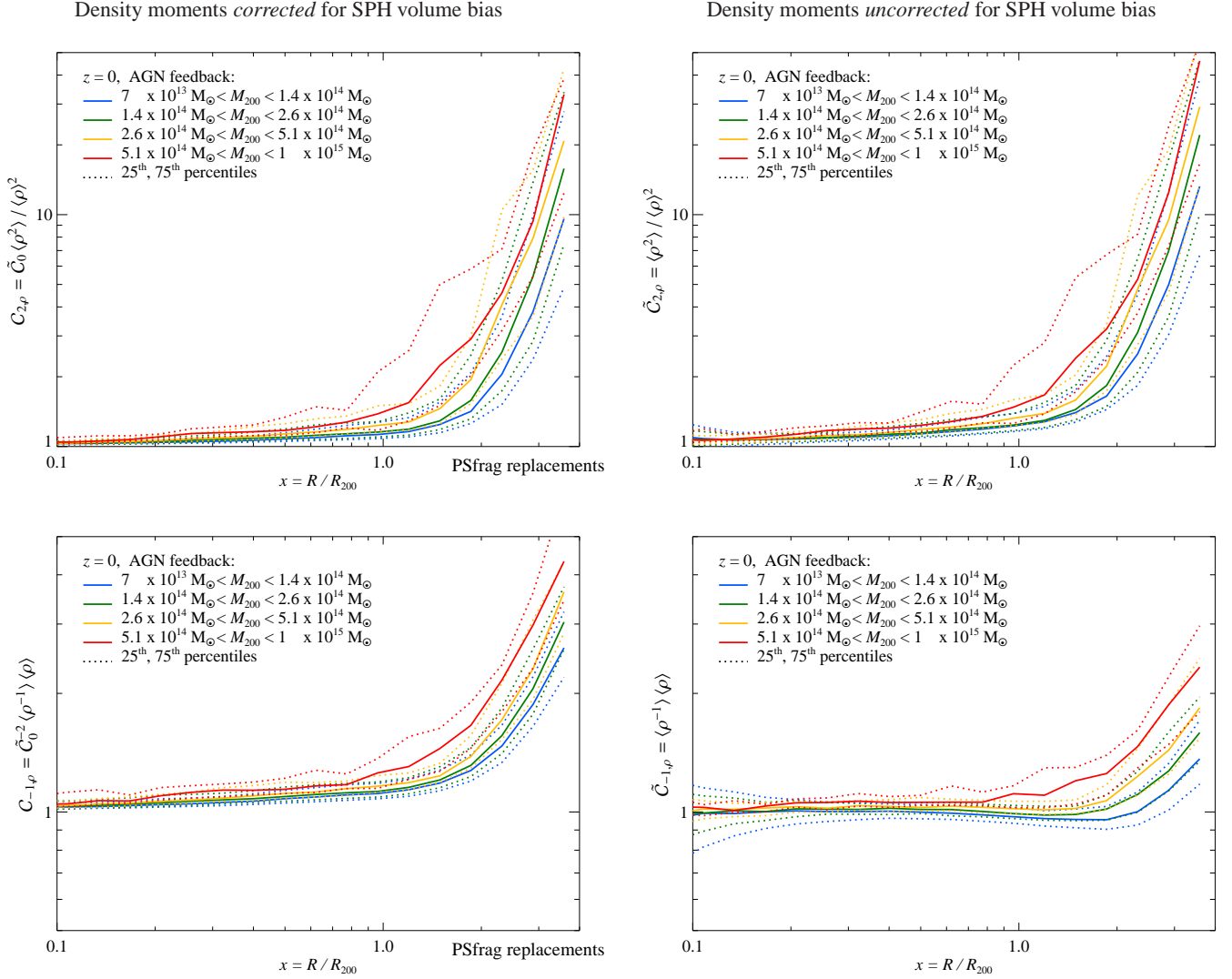


**Figure 16.** We compare density moments that are *corrected* for the SPH volume bias (left) with those that are *uncorrected* (right). Shown are median (solid) and 25<sup>th</sup>, 75<sup>th</sup> percentiles (dotted) for different cluster mass ranges (indicated with different colors). Upper panels show clumping factors  $C_{2,\rho}$ , and bottom panels the negative first order density moment  $C_{-1,\rho}$ . In the latter case, the SPH volume bias correction removes unphysical density moment estimates smaller than unity.

would artificially cut the colder pre-shock regions of the warm-

hot intergalactic medium  $T < 10^6$  K, introducing a progressively larger bias to smaller systems (see Figure 3).